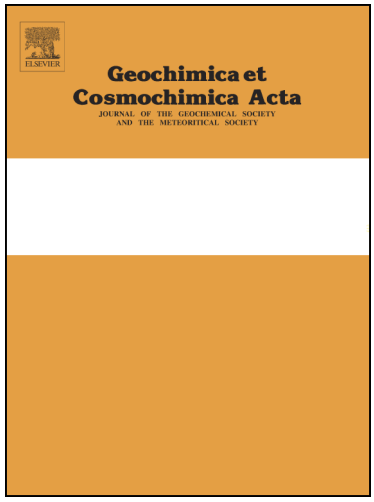

The effect of site geometry, Ti content and Ti oxidation state on the Ti K-edge XANES spectrum of synthetic hibonite

P.M. Doyle, A.J. Berry, P.F. Schofield, J.F.W. Mosselmans

PII: S0016-7037(16)30222-8
DOI: http://dx.doi.org/10.1016/j.gca.2016.05.001
Reference: GCA 9748

To appear in: *Geochimica et Cosmochimica Acta*

Received Date: 11 February 2015
Accepted Date: 1 May 2016

Please cite this article as: Doyle, P.M., Berry, A.J., Schofield, P.F., Mosselmans, J.F.W., The effect of site geometry, Ti content and Ti oxidation state on the Ti K-edge XANES spectrum of synthetic hibonite, *Geochimica et Cosmochimica Acta* (2016), doi: http://dx.doi.org/10.1016/j.gca.2016.05.001

The effect of site geometry, Ti content and Ti oxidation state on the Ti K-edge XANES spectrum of synthetic hibonite

P.M. DOYLE[1,2,†,*], A.J. BERRY[1,2,†], P.F. SCHOFIELD[2] AND J.F.W. MOSSELMANS[3]

[1] Department of Earth Science and Engineering, Imperial College London, South Kensington, London, SW7 2AZ, United Kingdom

[2] Department of Earth Sciences, Natural History Museum, South Kensington, London, SW7 5BD, United Kingdom

[3] Diamond Light Source Ltd, Diamond House, Harwell Science and Innovation Campus, Didcot, Oxfordshire OX11 0DE, United Kingdom

[†] P. Doyle is working at the Department of Geological Sciences, University of Cape Town, Rondebosch, 7701, South Africa. A. Berry is working at the Research School of Earth Sciences, Australian National University, Canberra, ACT 2601, Australia.

[*] Corresponding author e-mail address: p.doyle07@alumni.imperial.ac.uk

Abstract

The Al-rich oxide hibonite ($CaAl_{12}O_{19}$) is modelled to be the second mineral to condense from a gas of solar composition and is found within calcium-aluminum-rich inclusions and the matrix of chondritic meteorites. Both Ti^{3+} and Ti^{4+} are reported in meteoritic hibonite, so hibonite has been proposed as a single mineral oxybarometer that could be used to elucidate conditions within the first 0.2 Myrs of the Solar System.

Synthetic hibonites with $Ti^{3+}/(Ti^{3+}+Ti^{4+})$ (hereafter $Ti^{3+}/\Sigma Ti$) ranging between 0 and 1 were prepared as matrix-matched standards for meteoritic hibonite. The largest yield of both Ti-free and Ti-bearing hibonite at ~1300 and ~1400 ^{o}C was obtained by a single sinter under reducing conditions.

In situ micro-beam Ti K-edge X-ray absorption near edge structure (XANES) spectra were collected from the synthetic hibonites, as well as from terrestrial hibonite. Spectral features in the post-crest region were shown to correlate with the Ti^{4+} content. Furthermore, Ti^{4+} on the M2 trigonal bipyramidal and the adjoining M4 octahedral sites appears to cause variability in the post-crest region as a function of orientation. For this suite of synthetic hibonites it was observed that the pre-edge peak region is not influenced by orientation, but is controlled by $Ti^{3+}/\Sigma Ti$, site geometry and/or Ti concentration. In particular, the pre-edge peak

intensities reflect Ti coordination environment and distortion of the M4 octahedral site. Therefore, although pre-edge peak intensities have previously been used to determine $Ti^{3+}/\Sigma Ti$ in meteoritic minerals, we excluded use of the pre-edge peak intensities for quantifying Ti valence states in hibonite.

The energy of the absorption edge at a normalized intensity of 0.8 ($E_{0.8}$) and the energy of the minimum between the pre-edge region and the absorption edge (E_{m1}) were found to vary systematically with $Ti^{3+}/\Sigma Ti$. $Ti^{3+}/\Sigma Ti$ in hibonite as a function of E_{m1} was modelled by a quadratic function that may be used to quantify $Ti^{3+}/\Sigma Ti$ in meteoritic hibonite when the synthetic hibonite standards are crystal-chemically matched to the natural samples and are measured during the same analytical session as the meteoritic hibonites.

1. Introduction

Hibonite is found in the matrix of chondritic meteorites and in calcium-aluminum-rich inclusions (CAIs), the oldest Solar System materials dated (Connelly *et al.*, 2012). Many CAIs form by condensation and may then undergo multiple reprocessing events (Ireland, 1990) within the first 0.2 Myrs of the Solar System (Connelly *et al.*, 2012; Kita *et al.*, 2013). As such, the composition and textural relationships of hibonite can be used to elucidate early Solar System processes.

The refractory element Ti (Lodders, 2003) may be accommodated within the hibonite structure as both Ti^{3+} and Ti^{4+}, so hibonite is potentially a single-mineral oxybarometer (Beckett *et al.*, 1988). $Ti^{3+}/\Sigma Ti$ in hibonite may be determined stoichiometrically as Ti is often a major component within hibonite; Ti^{3+} substitutes directly for Al^{3+}, whereas Ti^{4+} undergoes a coupled substitution with Mg^{2+} for two Al^{3+} (Allen *et al.*, 1978) such that Ti in excess of the amount of Mg (Fig 1a) is inferred to be Ti^{3+}. Stoichiometric calculations are used for determining the Ti^{3+} content of fassaite (Haggerty, 1978; Simon *et al.,* 1991; Simon *et al.,* 2005; Grossman *et al.,* 2008; Dyl *et al.,* 2011). However, three reasons make it advantageous to measure the Ti^{3+}/Ti^{4+} ratio in hibonite directly. Firstly, the inclusion of additional redox-variable elements within meteoritic hibonites (*c.f.* Fig. 1b and 1c) complicates the stoichiometric calculation of $Ti^{3+}/\Sigma Ti$. Secondly, oxygen vacancies and/or cation defects (Beckett *et al.*, 1988) in a chemically complex mineral such as hibonite may compromise stoichiometric calculations. Thirdly, many meteoritic hibonite grains are very small (e.g. with diameters of <3 μm), making contamination of elemental analyses by underlying phases and/or by adjacent minerals sometimes unavoidable (e.g., Weber and Bischoff, 1994).

$Ti^{3+}/\Sigma Ti$ has previously been determined for glasses and meteoritic hibonite using bulk analysis techniques such as titration (Schreiber *et al.*, 1978; Tranell *et al.*, 2002) and electron spin resonance (ESR) spectroscopy (Beckett *et al.*, 1988), respectively. Titration is suitable for analysis of Fe-free compositions, but produces anomalously high $Ti^{3+}/\Sigma Ti$ values in Fe-bearing systems, as shown by Whipple (1979). ESR spectroscopy is restricted to the analysis of paramagnetic elements, so $Ti^{3+}/\Sigma Ti$ is determined by measuring the concentration of Ti^{3+}. Furthermore, ESR spectra may be complicated by the presence of other paramagnetic elements (Schreiber *et al.*, 1978) and are interpreted in light of available structural data. For example, of the five Al sites in hibonite, Beckett *et al.* (1988) inferred from ESR spectra that Ti^{3+} occupied the M2 trigonal bipyramidal site, a key requirement for their proposed oxybarometer. However, a recent neutron powder diffraction (NPD) study by Doyle *et al.* (2014) showed that Ti^{3+} does not occupy the M2 site, but instead occupies the M4 octahedral site, and Ti^{4+} partitions between the M2 trigonal bipyramidal site and the M4 octahedral site.

Spectroscopic techniques such as X-ray absorption near edge structure (XANES) spectroscopy and electron energy-loss spectroscopy (EELS) may be used to determine the ratio of oxidation states for redox-variable elements directly as both methods explore the electronic structure of an atom. These techniques offer μm to nm spatial resolution (Smith *et al.*, 2004; Schofield *et al.*, 2010), are element-specific and are applicable to a range of elements, e.g., Ti (Stoyanov *et al.*, 2007; Waychunas, 1987) and Fe (van Aken and Liebscher, 2002; Berry *et al.*, 2008).

Approximately 100 nm thick sections are required for EELS analysis, for which focused ion beam (FIB) sections are extracted from polished sections. So, whether or not the samples are stable during EELS analysis, the sample preparation required for EELS is destructive. In contrast, XANES spectra can be collected from samples mounted as unpolished grains or (preferably) polished sections prepared for optical and electron microscopy. As no additional sample preparation is required before XANES analysis, it can be considered a non-destructive technique (Schofield *et al.*, 2010, 2014), which is beneficial when analyzing unique samples and samples on loan from museums and personal collections.

Ti K-edge X-ray absorption spectra are divided into four main regions, namely the pre-edge, absorption edge and post-crest regions (the XANES region) and the extended X-ray absorption fine structure (EXAFS) region. The pre-edge feature is particularly sensitive to oxidation state as it results from $1s \rightarrow 3d$ electronic transitions between the K-shell and empty (or partially filled) bound states when the target element is in a distorted site. Similarly, to a first-order approximation, the absorption edge-energy of a redox-variable

element will be dependent on its oxidation state as core electrons are bound more tightly in higher oxidation states than in lower oxidation states (Brown *et al.*, 1988). Indeed, the energy of pre-edge and absorption edge features in Ti K-edge XANES spectra collected from Ti^{3+}-bearing phases were reported to be ~2 eV lower than those collected from similar Ti^{4+}-bearing phases (Waychunas, 1987). A shift to higher energy with higher oxidation state has also been documented for pre-edge or absorption edge features in spectra of V^{2+}-V^{5+} (Sutton *et al.,* 2005), Cr^{2+}/Cr^{3+} (Berry and O'Neill, 2004), Fe^{2+}/Fe^{3+} (Berry *et al.*, 2003), and Eu^{2+}/Eu^{3+} (Burnham *et al.,* 2015).

Ti K-edge XANES spectra have been recorded for Ti^{3+}- and Ti^{4+}-bearing glasses (Yang *et al.,* 2008; Krawczynski *et al.*, 2009), synthetic garnet (Krawczynski *et al.*, 2009) and meteoritic olivine, pyroxene, spinel and hibonite (Simon *et al.*, 2007a,b, 2009; Paque *et al.*, 2013). $Ti^{3+}/\Sigma Ti$ has been quantified previously using either Ti^{3+}- and Ti^{4+}-bearing pyroxenes (Simon *et al.*, 2007a) or a mixing triangle defined by structurally diverse end-members (Krawczynski *et al.*, 2009; Simon *et al.*, 2007b, 2009). The Ti K-edge XANES study by Waychunas (1987) also sought to quantify the Ti^{3+}-content of silicates, but reported the results as semi-quantitative "at best" as shifts due to coordination, site symmetry and composition could not be separated adequately from shifts in energy due to valence state. In particular, the pre-edge feature is strongly affected by Ti coordination (Farges *et al.*, 1996), and Ti^{4+} can occur in tetrahedral, square pyramidal, trigonal bipyramidal and octahedral coordination (Farges *et al.*, 1996). It therefore seems wise to heed the caution of Waychunas (1987) that "standards of similar structure and composition" are needed in order to determine ratios of redox-variable elements quantitatively. This study reports a means of quantifying $Ti^{3+}/\Sigma Ti$ in hibonite using Ti K-edge XANES spectra collected from a suite of well-characterized synthetic hibonite samples with $Ti^{3+}/\Sigma Ti$ ranging from 0 to 1.

2. Samples and Analytical Techniques

2.1. Synthesis

Hibonite structure **–** Hibonite is structurally complex, having five Al sites (Supplementary Fig. 1) onto which Ti may substitute: one trigonal bipyramidal site (M2), one tetrahedral site (M3) and three octahedral sites (M1, M4, M5). The site multiplicity (subscript) and coordination number (superscript) of hibonite may be summarized as $^{[12]}Ca^{[6]}M1^{[5]}M2^{[4]}M3_2^{[6]}M4_2^{[6]}M5_6O_{19}$ (after Bermanec *et al.*, 1996).

A recent NPD study showed that Ti^{3+} only occupies the M4 octahedral site, whereas Ti^{4+} partitions between the M2 trigonal bipyramidal site and the M4 octahedral site in a roughly

constant ratio of 0.18, irrespective of the Ti and Ti^{3+} contents (Doyle *et al.*, 2014). Ti^{4+} undergoes a coupled substitution with Mg^{2+} in order to maintain charge balance (Allen *et al.*, 1978), and Mg^{2+} occupies the M3 tetrahedral site (Doyle *et al.*, 2014).

Ti-free hibonite and Ti saturation series – Ti-free hibonites were prepared using a range of different conditions, as summarized in Supplementary Table 1. In order to investigate Ti-saturation in hibonite, a suite of Ti^{3+}- and Ti^{4+} end-member compositions were prepared from stoichiometric mixtures of oxides at ~1400 °C and 1 atm, with up to 125% Ti saturation, as predicted by the reported site occupancies of Ti^{3+} and Ti^{4+} (Beckett *et al.* 1988; Bermanec *et al.* 1996). Considering the reported site multiplicity of the M2 and M4 sites, the Ti contents of the Ti^{3+} and Ti^{4+} end-member hibonite series ranged up to 14 and 28 wt% TiO_2, respectively.

Stoichiometric mixtures were prepared using pre-dried $CaCO_3$, Al_2O_3, TiO_2 and MgO. The oxide powders were pressed into pellets and heated in a 1 atm vertical tube furnace equipped with CO and CO_2 mass flow controllers to control the oxygen fugacity (fO_2). The hibonite samples were synthesized at ~1400 ºC, which is within the stability field of hibonite at low pressure (Yoneda and Grossman, 1995) and well below the experimentally determined incongruent melting temperature of hibonite (1850 ±10 °C in the CaO-MgO-Al_2O_3±SiO_2 system; De Aza *et al.*, 2000; Vázquez *et al.*, 2003). The Ti^{3+} end-member hibonite compositions ($Ti^{3+}/\Sigma Ti$ = 1) were held in graphite in CO at logfO_2 = -16 (iron-wüstite (IW) -6.5), and the Ti^{4+} end-member hibonite compositions ($Ti^{3+}/\Sigma Ti$ = 0) were suspended in a Pt crucible in either air (IW+8.8) or CO_2 (IW+6.5). For samples that were re-sintered, the primary product was powdered by crushing in a pellet die and ground by hand using an agate pestle and mortar. Up to two sinters were made of the Ti^{3+} end-member hibonites, all of which were extracted into air at ambient room temperature from 600 °C. The Ti^{4+} end-member hibonites were sintered four times, with the first three sinters being extracted into air at ambient room temperature after cooling to 600 °C, and the fourth being quenched into water from ~1400 °C.

Ti valence state series - The results of the saturation series experiments and the reported Ti contents of meteoritic hibonites (Fig. 1) governed the choice of compositions for a synthetic hibonite series with $Ti^{3+}/\Sigma Ti$ ranging between 0 and 1. Large volumes (>5 g) of two Ti^{3+} end-member hibonites and two Ti^{4+} end-member hibonites were prepared, as well as a suite of mixed-valent samples. One of the mixed-valent samples was an analogue of hibonite from the pleochroic blue aggregate (BAG) CAI 10-43 in the CM2 Murchison chondrite.

Stoichiometric mixtures of pre-dried oxides were prepared for sintering at ~1400 °C, as

described above. The Ti^{3+} end-member hibonites and the mixed-valent samples were mounted in graphite and prepared at IW-6.5, relying on the MgO content of the stoichiometric mixture to control $Ti^{3+}/\Sigma Ti$ (noting the coupled substitution of Ti^{4+} and Mg^{2+}). Two Ti^{4+}-hibonite compositions ($Ti^{3+}/\Sigma Ti = 0$) were each suspended in a Pt crucible at $\log fO_2$ = -3 (IW+6.5) and re-sintered (following regrinding and X-ray powder diffraction (XRD) analysis) for ~32 h respectively. All synthesis products were cooled to 600 ºC, taking approximately 2 h before the samples were removed from the furnace.

2.2. Characterization

Diffraction – Phase identification was made using XRD data collected with a Nonius PDS 120 powder diffraction system (Cu $K\alpha_1$ radiation) fitted with an Inel curved, position sensitive detector (e.g., Schofield *et al*., 2002). A subset of eight samples was further characterized by NPD (Doyle *et al.,* 2014).

Electron microscopy – The hibonite compositions were determined by energy dispersive spectroscopy (EDS) using a 5900LV JEOL scanning electron microscope (SEM) operating at 10 kV and 2 nA. The voltage was lower than commonly used, and the resulting smaller excitation volume allowed ~100 wt% totals to be obtained from the platy hibonite crystals (Fig. 2). The fluorescence was calibrated to the K-lines of Mg and Si in $Mg_{1.6}Fe_{0.4}SiO_4$, Ca in $CaSiO_3$, Al in Al_2O_3, and Ti in TiO_2 rutile. Matrix corrections were made using the Oxford Instruments XPP routine. Although wavelength dispersive spectrometry potentially provides more accurate analyses, EDS is sufficiently accurate for the purpose of this study given the range of compositions observed for some samples (Table 1).

The Ti content is reported as TiO_2 (Table 1), which would result in an overestimation of the proportion of oxygen if Ti^{3+} (nominally as Ti_2O_3) substituted directly for Al^{3+} without the creation of oxygen vacancies. That being the case, if the oxide wt% totals of the Ti^{3+}-bearing hibonites are ~100, then the number of cations (determined from elemental wt%) would be less than 13. Indeed, the number of cations in the formulae of the Ti^{3+}-bearing hibonites (12.91-12.95 pfu) is less than that of the Ti^{4+} end-member hibonites (12.98-13.01 pfu).

Ti valence state – The $Ti^{3+}/\Sigma Ti$ values of the synthetic hibonites are crucial for the results of this study. As the starting stoichiometry of the samples was known to be free of other mixed-valent elements, $Ti^{3+}/\Sigma Ti$ was determined by stoichiometry, with $1Ti^{4+}$:$1Mg^{2+}$ and the remaining Ti as Ti^{3+}. The compositions that do not contain Mg are therefore expected to have $Ti^{3+}/\Sigma Ti = 1$.

$Ti^{3+}/\Sigma Ti$ was calculated using 26 – 42 point analyses (Table 1). The resulting average $Ti^{3+}/\Sigma Ti$ values are equal to those calculated from the stoichiometries of the starting

compositions. Moreover, the $Ti^{3+}/\Sigma Ti$ determined by stoichiometry is consistent with the results of the Rietveld refinement of NPD data. Indeed, as Ti^{4+} partitions into the M2 trigonal bipyramidal site and the M4 octahedral site (Doyle *et al.*, 2014), Ti^{4+} would have been refined onto the M2 site in the Ti^{3+} end-member hibonites had Ti^{4+} been present. This was not found to be the case for the two Ti^{3+} end-member hibonites, for which Rietveld refinement of all the Ti onto the M4 site provided the best fits to the NPD data.

The $Ti^{3+}/\Sigma Ti$ determined by stoichiometry may further be checked by normalizing the hibonite formulae to 13 cations. This method was employed by Simon *et al.* (1997), who showed that "normalizing to 13 cations yields almost exactly 19 O anions", from which they concluded that direct substitution of Ti^{3+} for Al^{3+} occurred without the need for the reduction of Ti^{4+} and simultaneous creation of oxygen vacancies. Herein the proportion of oxygen was recalculated from the $Ti^{3+}/\Sigma Ti$ determined by stoichiometry and ΣTi determined by EDS, assuming Ti^{3+} as Ti_2O_3 and Ti^{4+} as TiO_2. Doing so results in 13.0 (12.98-13.03) cations per formula unit (pfu) when normalized to 19 O; and 19.0 (18.96-19.03) O pfu when normalized to 13 cations. Following the argument of Simon *et al.* (1997), we therefore deduce that the $Ti^{3+}/\Sigma Ti$ values reported for the samples in this manuscript are correct, and that Ti^{3+} substituted directly for Al^{3+} without the need for cation vacancies.

Throughout this text, the samples will be identified by reference to their Ti pfu and their $Ti^{3+}/\Sigma Ti$ ratio in the form (Ti pfu, $Ti^{3+}/\Sigma Ti$). For example, sample (0.5,1) would have 0.5 Ti pfu with all the Ti trivalent, giving a stoichiometry of $CaAl_{11.5}Ti_{0.5}O_{19}$. Sample (1,0) would have 1.0 Ti^{4+} pfu and 1.0 Mg^{2+} pfu, giving a stoichiometry of $CaAl_{10.0}Ti_{1.0}Mg_{1.0}O_{19}$.

2.3. XANES analysis

Samples and mounting **–** Well-characterized Ti-bearing materials were used as standards. These included Ti^{4+} oxide (SpecPure $^{[6]}TiO_2$ (rutile); Johnson Matthey), $^{[6]}Ti^{3+}$-oxide (99.9 % pure Ti_2O_3; Sigma Aldrich), Ti-spinel ($Ni_{2.62}{}^{[4]}Ti_{0.69}O_4$; Berry *et al.*, 2007) and Ti-olivine ($Mg_{2.00}{}^{[4]}Ti_{0.01}Si_{0.99}O_4$; Berry *et al.*, 2007). The analytical grade oxides were mixed with BN powder and pressed to form pellets such that the Ti content was 1 mol%, and the Ti-spinel and Ti-olivine were mounted as polycrystalline pieces in epoxy resin.

During a preliminary study, Ti K-edge XANES spectra were collected from synthetic hibonite powder pellets that were prepared such that the samples were either undiluted or diluted to 1 mol% Ti in BN. An example of these spectra, shown for two Ti^{3+} end-member hibonites, is shown in Supplementary Fig. 2. The Ti valence state calibration investigation is based on a follow-up study in which Ti K-edge XANES spectra were collected from a subset

of the sintered synthetic hibonite samples that were mounted in epoxy resin and polished for electron microscopy.

As hibonite is an anisotropic mineral, Ti K-edge XANES spectra were collected from natural and synthetic hibonite crystals in order to investigate the effect of orientation on spectral features. In particular, a crystal of terrestrial hibonite (BM 1966,28c), mounted in epoxy resin, was attached to an orientated stage so that spectra could be collected at discreet angles. In addition, spectra were collected from multiple randomly oriented hibonite crystals within epoxy-mounted sintered products.

Measurement **-** Ti K-edge XANES spectra were recorded in fluorescence mode at beamline i18 (undulator source) at the Diamond Light Source (DLS) Oxfordshire, UK (Mosselmans *et al*., 2009). The excitation energy was selected using a Si(111) monochromator and calibrated by defining the first derivative peak in the Ti K-edge XANES transmission spectrum of Ti foil to be 4966.4 eV (Bearden and Burr, 1967). The beam was collimated by a toroidal mirror and defined by vertical and horizontal slits (Mosselmans *et al*., 2008, 2009). Thereafter, the beam was focused onto the sample using Kirkpatrick-Baez (KB) mirrors, which produced a 2 x 2 μm spot. Fluorescence was measured using a nine-element monolithic germanium detector, with the total incoming count rate of ~ 130000 cts/s. The sample and detector were orientated at 45^{o} and 90^{o}, respectively, to the incident beam, resulting in a beam footprint of ~2 x 3 μm on the sample.

The step sizes used to collect data from hibonite were as follows: 0.5 eV between 4950 and 4960 eV (background), 0.1 eV between 4960 and 4975 eV (pre-edge region), 0.2 eV between 4975 and 5015 eV (edge, crest and post-crest region) and 2.5 eV up to 5200 eV (EXAFS region) such that the total scan time was ~20 min. Six to ten Ti K-edge XANES spectra were collected from each of the synthetic hibonite samples used for the $Ti^{3+}/\Sigma Ti$ valence state calibration.

Data processing – Deadtime-corrected fluorescence data from the nine detector channels were averaged and normalized to the incident beam flux. A linear background was subtracted from the Ti_2O_3 spectrum by fitting a line through the 5070-5095 eV EXAFS region. This step was not necessary for the spectra collected from any of the other samples as their pre-edge and EXAFS regions were horizontal. Following Berry *et al*. (2007), therefore, a constant background was subtracted, after which the spectra were normalized to the absorption edge jump as defined by the average intensity of the EXAFS region above 5145 eV.

The energy resolution of the beamline at the energy of the Ti K-edge is 0.70 eV, resulting in a spectral energy resolution of 1.2 eV when coupled with the Ti Kα core-hole

width of 0.94 eV (Krause and Oliver, 1979). The absorption length of the incident X-rays for the range of hibonite compositions was calculated to be 10 – 13 μm (after Henke *et al*., 1993).

There is no evidence for self-absorption influencing the spectra for a suite of synthetic hibonite samples with Ti contents ranging from 1 mol% Ti (BN-diluted hibonite powders) to 11.4 wt% TiO_2 (sintered and powdered hibonite). Indeed, as noted by Doyle (2012), similar lineshapes were observed for spectra collected from synthetic hibonite mounted in three ways: epoxy-resin mounted sintered pellets (micro-focus beam), hibonite powder pellets (diffuse beam) and BN-diluted hibonite powders (diffuse beam).

The pre-edge regions of the spectra were modelled using PeakFit v4. The background was modelled by fitting two peaks to the edge, one to model the rising absorption edge and one to account for a shoulder (b_{fit1}); the pre-edge feature was fitted using three or four peaks with peak widths constrained to be constant for each sample across the series. All peaks were modelled as Gaussian-Lorentzian Cross Product (Amplitude) functions. Example fits are provided in Supplementary Figure 3.

3. Results

3.1. Synthetic products

Ti-free hibonite – Impurities were found in all of the Ti-free sinter products, irrespective of fO_2 (IW+6.5, IW−2.5, IW−6.5), temperature (1300 and ~1400 °C), and sample preparation method employed (single or multiple sinter(s), air-extraction or water quench). In particular, corundum (Al_2O_3) was observed in all samples. A few run products contained $CaAl_4O_7$ (grossite) and/or a minor amount of $Ca_3Al_{10}O_{18}$. The largest hibonite yield was produced under reducing conditions (IW-2.5), whereas the sample with the most Al_2O_3 was produced under oxidizing conditions (IW+6.6).

Ti Saturation series – Samples prepared under reducing conditions produced almost pure hibonite after one sinter. In contrast, the yield of Ti^{4+} end-member hibonites was maximized after two sinters.

The Ti^{3+} hibonites were sky-blue in color where exposed to the gas and discolored (greyish) where enclosed by graphite. The Ti^{4+} hibonite saturation-series samples were white. This coloration is consistent with Ti^{3+} being present (blue) or absent (white) according to studies by Ihinger and Stolper (1986) and Beckett *et al.* (1988).

No impurities were identified in the XRD patterns for Ti^{3+} end-member hibonites with starting compositions having ≤0.75 Ti^{3+} pfu, but Al_2O_3 and minor amounts of a Ti-oxide, which could not be identified from the stoichiometry, were noted by EDS SEM analysis. $CaTiO_3$ (perovskite) was found in the Ti-rich sample (1,1) by XRD and EDS SEM. Impurities such as $CaTiO_3$ ±$MgAl_2O_4$ (spinel) ±Al_2O_3 ±Mg-Al-Ti-oxide were noted in the Ti^{4+} end-member hibonites with >1Ti pfu. As significant quantities of impurities were noted in samples with ≥0.75 Ti^{3+} pfu and >1 Ti^{4+} pfu, the end-member and mixed-valent hibonites used in the XANES study were made from compositions with ≤0.5 Ti^{3+} pfu and ≤1 Ti^{4+} pfu.

Ti valence state series – The Ti^{3+} end-member hibonites and the mixed-valent hibonites were blue in color, with grey discoloration in the areas shielded by graphite. The Ti^{4+} hibonite sinter products were white.

Backscatter electron imaging (BEI) of polished samples mounted in epoxy resin revealed that the sintered products were highly porous aggregates of crystals ~10 μm in the longest dimension. The porosity of the single-sintered Ti^{3+}-bearing hibonites was greater than that of the twice-sintered Ti^{4+} hibonites (Fig. 2).

The Ti contents of the series range from 2.4 to 11.4 wt% TiO_2, translating into 0.20 to 0.98 Ti pfu (Table 1). The Ti^{3+} and Ti^{4+} end-member hibonites (0.20,1), (0.33,1) and (0.98,0) were compositionally homogeneous (±0.04–0.06 Ti pfu), as were the mixed-valent hibonites (0.62,0.60) and (0.73,0.33).

The Ti^{4+} end-member hibonite (0.44,0) has TiO_2 contents ranging from 2.7 to 7.2 wt%, with crystal compositions trending along the 1Ti:1Mg line (Fig. 1a), resulting in a large uncertainty associated with the Ti content (±0.12 Ti pfu) and calculated $Ti^{3+}/\Sigma Ti$ value. Indeed, although the average calculated $Ti^{3+}/\Sigma Ti$ is zero, the uncertainty on $Ti^{3+}/\Sigma Ti$ is ±0.14, which is much larger than the value of ± 0.05 found for the Ti-rich Ti^{4+} end-member (0.98,0). The uncertainties reflect the compositional spread in (0.44,0) and the experimental error associated with EDS SEM for both samples (Table 1).

The mixed-valent sample (0.46,0.10), which was prepared as a natural analogue to hibonite in the Murchison CAI 10-43 (Ireland, 1988) is blue in color and has a $Ti^{3+}/\Sigma Ti$ value of 0.10±0.12. The hibonite crystals have TiO_2 contents ranging from 2.3 to 7.6 wt%, with scatter along the 1Ti:1Mg line. Due to the large uncertainty associated with the calculated $Ti^{3+}/\Sigma Ti$ value and similarity of the composition to that of the Ti^{4+} end-member (0.44,0), XANES spectra were not recorded for this sample.

The synthetic hibonite compositions are all similar to those of the starting mixtures. Indeed, the Ti content of (0.62,0.60) suggests a product purity of 99%, assuming ideal

stoichiometry of the starting composition, and Al_2O_3 was the only impurity detected by NPD in the Ti^{3+}-bearing samples (0.20,1), (0.33,1) and (0.73,0.33). The presence of trace Al_2O_3 in the blue regions of the Ti^{3+}-bearing hibonites was confirmed by SEM. Trace amounts of an unidentified Ti-oxide were found within the greyish regions of these three samples, and may potentially be responsible for this discoloration. The greyish discoloration would be consistent with the presence of Ti in a reduced form, perhaps as TiO (MSDS). Where possible, the samples were mounted such that the pure-blue regions (up to 13 mm in diameter) were exposed on the polished surface of the epoxy resin mounts. XANES spectra could therefore be collected from regions free of Ti-oxide impurities.

Ti-free spinel ($MgAl_2O_4$) was identified in the two Ti^{4+} end-member hibonites (0.44,0) and (0.98,0), but would not affect Ti K-edge XANES spectra. Perovskite ($CaTiO_3$) was found in (0.98,0) by NPD and EDS, and trace amounts of $CaTiO_3$ were found by EDS in (0.44,0). As perovskite occurs in discrete regions <10 μm in size (Fig. 2), perovskite-rich regions could be avoided by the 2×2 μm sized X-ray beam. It is possible that perovskite could be sampled sub-surface as the absorption length for the incident X-ray beam in hibonite is calculated to be 10 - 13 μm (after Henke *et al.*, 1993). However, if perovskite (~59 wt% TiO_2) was sampled, its characteristic line-shape would be evident in the hibonite spectra (Doyle, 2012).

3.2. XANES spectroscopy

Ti-bearing reference materials **–** Ti K-edge XANES spectra were collected from four reference materials. The spectra are shown in Fig. 3, with features in the pre-edge (a_1, a_2, a_3), absorption edge (b_1, b_2, b_3), crest (c) and post-crest (d_1, d_2, d_3) marked. Up to three peaks are identified in the post-crest region, and the lineshapes are similar to those reported previously for TiO_2, Ti_2O_3 (Waychunas, 1987), Ti-olivine and Ti-spinel (Berry *et al.*, 2007). The energy of the Ti_2O_3 absorption edge is lower than that of the Ti^{4+}-bearing Ti-olivine, Ti-spinel and TiO_2, consistent with the findings of Waychunas (1987).

A single, intense pre-edge peak was observed in the spectra collected from four-fold coordinated Ti^{4+} ($^{[4]}Ti^{4+}$) in olivine ($^{[4]}$Ti-ol) and spinel ($^{[4]}$Ti-sp), whereas three less-intense pre-edge peaks were observed for six-fold coordinated Ti^{4+} in rutile ($^{[6]}TiO_2$). The sensitivity of the Ti^{4+} pre-edge peak to coordination environment allows energy and intensity fields to be defined (Farges *et al.*, 1996). The pre-edge peak energy and intensity of $^{[4]}$Ti-sp and $^{[6]}TiO_2$ fit well within the four- and six-fold coordination fields respectively. The pre-edge peak intensity of $^{[4]}$Ti-ol matches that of Berry *et al.* (2007) and plots slightly above the field described in Farges *et al.* (1996). The a_2 pre-edge peak intensity of $^{[6]}Ti_2O_3$ lies within the

intensity range of $^{[6]}Ti^{4+}$, but the energy of the $^{[6]}Ti^{3+}$ pre-edge is 0.6 eV lower than that of $^{[6]}Ti^{4+}$. The linear background applied to the spectrum collected from Ti_2O_3 influenced the intensity of the pre-edge peak, but the energy of the inflection point of the first derivative for the spectrum is constant for different backgrounds.

Synthetic hibonite – As shown in Figure 4, four peaks (d_1-d_4) are observed in the post-crest region of the average spectra collected from the Ti^{4+} end-member hibonites (0.44,0) and (0.98,0). The d_2 peak is less evident in the mixed-valent hibonite spectra and absent in the Ti^{3+} end-member hibonite spectra.

There are three distinct peaks in the pre-edge region of the Ti^{4+} end-member hibonite spectra, although a small additional peak was required for the best spectral fitting (Supplementary Fig. 3). The a_3 peak in spectra collected from (0.98,0) is more intense than the a_3 peak in spectra collected from (0.44,0). Three distinct peaks are also evident in the Ti^{3+}-bearing hibonite spectra, and the lineshapes of the spectra collected from two Ti^{3+} end-member hibonites (0.20 and 0.33 Ti^{3+} pfu) are similar (Supplementary Fig. 2). Spectra collected from minerals such as ilmenite, anatase and rutile, with Ti in distorted octahedral coordination, are reported to have three peaks in the pre-edge region (Waychunas, 1987; Farges *et al.*, 1996), so the presence of three peaks in the pre-edge region of both Ti^{4+} and Ti^{3+} end-member hibonite spectra might suggest that the Ti is predominantly in octahedral coordination. This is consistent with the mechanism for Ti substitution in hibonite (Doyle *et al.*, 2014) in which the overwhelming majority of Ti occupies the octahedral M4 site.

Ti^{4+} also occupies the M2 trigonal bipyramidal site ($^{[5]}Ti^{4+}_{[M2]}$), but as the proportion of this species is only ~14% in the Ti^{4+} end member hibonites (calculated from Doyle *et al.*, 2014), any potential additional peaks in the pre-edge region may be difficult to observe, especially if they overlap with peaks associated with Ti^{4+} in octahedral coordination. However, the a_2 peak is more intense in the spectra collected from the Ti^{4+}-bearing hibonites than in spectra collected from the Ti^{3+} end-member hibonites. The enhanced intensity of this peak may be attributed to Ti^{4+} occupying the M2 trigonal bipyramidal site ($^{[5]}Ti^{4+}_{[M2]}$). The a_2 peak of the Ti^{4+} end-member hibonite with 0.44 Ti^{4+} pfu is equal in intensity (within uncertainty) to that for the 0.98 Ti^{4+} end-member hibonite. For the Ti^{3+}-bearing hibonites, however, the intensity of the a_2 pre-edge peak is non-linearly correlated in a negative manner with $Ti^{3+}/\Sigma Ti$ (Fig. 4) and positively with Ti pfu (Fig. 5a).

The shape of the absorption edge changes as a function of $Ti^{3+}/\Sigma Ti$. The spectral intensities were all normalized such that the EXAFS region averaged one. The crest intensities are greater than one, and in our samples a normalized intensity of 0.8 avoids

intersection with the b_{1-3} shoulders, which do not appear to change systematically as a function of $Ti^{3+}/\Sigma Ti$. The energy at which the absorption edge intensity equals 0.8 ($E_{0.8}$) was selected to quantify how the absorption edge varies with $Ti^{3+}/\Sigma Ti$. The $E_{0.8}$ values are given in Table 2.

The energy of the m_1 minimum (E_{m1}) between the pre-edge and the absorption edge changes as a function of $Ti^{3+}/\Sigma Ti$ (Table 2). The position of E_{m1} is most easily determined for samples with >1 wt% TiO_2 (Doyle, 2012) from the first derivative of the spectrum (Supplementary Fig. 4). In hibonites with <1 wt% TiO_2, the signal to noise ratio is low (Doyle, 2012), but E_{m1} may be obtained by fitting a second order polynomial through a subset of the data.

Orientation study **–**Terrestrial hibonite includes several additional trace elements (e.g. Bermanec *et al.*, 1996) that are not present in hibonites found in CAIs, and consequently it is not a good analogue for meteoritic hibonite. Nevertheless, terrestrial hibonite crystals from Madagascar (the type area) are large and platy: a crystal ~1.5 × 2 mm in size was mounted in an epoxy resin disk with the c-axis normal to the polished surface. The stage was rotated in the plane of the polished surface and spectra were collected at angles of 0^o, 30^o and 45^o. As the polarized X-ray beam was orientated at 45^o to the polished surface, it would enter the structure between the a- and c- axes. However, no orientation dependence was observed in these spectra (Supplementary Fig. 5).

The purity of the synthetic samples (Fig. 2) means that spectra of hibonite, without contributions from other phases, were recorded. Therefore, between 6 and 10 spectra were recorded from random points on the synthetic hibonite samples such that each spectrum would correspond to a hibonite crystal (or possibly several crystals) in a different orientation.

In 10 spectra from the (0.44,0) Ti^{4+} end-member hibonite the d_3 peak intensity and the intensity of the m_3 minimum in the post-crest region both vary (Supplementary Fig. 5). In contrast, equivalent features in the post-crest region of the Ti^{3+} hibonite (0.20,1) do not vary significantly. The results suggest that this multi-spot orientation study is sufficiently sensitive to detect orientation effects in Ti K-edge XANES spectra of synthetic hibonites. The pre-edge features of both the Ti^{3+} and Ti^{4+}-bearing hibonites exhibit little dependence on orientation (Supplementary Fig. 5). Indeed, the energies of the a_2 peak and m_1 minimum vary by ≤0.1 eV in the replicate spectra collected from each sample (Table 2), and the intensity of the a_2 peak varies by ±0.01 (≤6.4% of the average intensity).

4. Discussion

4.1. Synthesis of hibonite

Influence of fO_2 – The largest yield of Ti-free hibonite was obtained under reducing conditions. To maximize the yield of Ti-bearing hibonites prepared under oxidizing conditions a second sinter was always required. The yield of Ti-bearing hibonites produced in a single sinter under reducing conditions was always higher than that prepared under oxidizing conditions, and this remained the case even when the Ti-bearing hibonites prepared under oxidizing conditions were sintered for a second time. Domínguez *et al.* (2001) noted that hibonite is more stable under reducing conditions and our results suggest that the crystallization and reaction kinetics for the preparation of Ti-free and Ti^{3+}-bearing (including mixed valent) hibonite from oxide mixtures may be enhanced under reducing conditions.

The presence of Al_2O_3 and $CaAl_4O_7$ in the Ti-free hibonite samples is consistent with the reaction for the formation of hibonite from oxides given by Domínguez *et al.* (2001):

$$CaCO_3 + Al_2O_3 \rightarrow CaO + Al_2O_3 + CO_{2\,(g)} \quad \text{(Calcination reaction ~848 °C)} \qquad \text{Equation 1}$$

$$\textit{then:}\ CaO + 6Al_2O_3 \rightarrow CaAl_2O_4 + 5Al_2O_3 \rightarrow CaAl_4O_7 + 4Al_2O_3 \rightarrow CaAl_{12}O_{19} \qquad \text{Equation 2}$$

Pure hibonite is notoriously difficult to synthesize (Hofmeister *et al.*, 2004; Callender and Barron, 2000). Al_2O_3 is a common impurity in syntheses, regardless of the method employed (Holtstam, 1996; Callender and Barron, 2000; Vázquez *et al.*, 2003). Whereas powdering and resintering material may be expected to increase sample purity, refractory phases such as Al_2O_3 can persist even after many resinters. Indeed Al_2O_3 impurities remained even after four sinters. Similarly, despite nine sinters at 1500-1625 °C and a product that appeared to be pure by XRD analysis, Geiger *et al.* (1988) still found traces of Al_2O_3 in their samples using SEM analysis. The stability of the simple oxide phases (e.g. Al_2O_3) in the starting compositions likely contributes to the abundance of impurity phases (Hofmeister *et al.*, 2004).

Crystal morphology – Hibonite has a hexagonal crystal form, and this can be observed clearly in the platy Ti^{3+}-bearing samples (e.g. Fig. 2b). In contrast, the Ti^{4+} end-member hibonite crystals are predominantly tabular in form. The mixed-valent hibonite crystals are intermediate, having an elongated hexagonal form compared to the crystals of the Ti^{3+} end-member hibonites (Doyle *et al.*, 2012).

Incorporation of Ti^{4+} (and not Ti^{3+}) on the M2 site, along with Mg^{2+} on the M3 site, may alter the form of Ti^{4+}-bearing hibonite crystals, accounting for the elongate crystals observed in the Ti^{4+} end-members and the mixed-valent hibonite charges. Similarly, in a synthetic

system in which Fe^{2+} is incorporated into the hibonite structure by coupled substitution with Ti^{4+}, the hibonite crystals are reported to be tabular in form (Holtstam, 1996).

4.2. Structural control of Ti K-edge XANES spectra

Before investigating spectral variations due to the oxidation state of Ti, the spectra of synthetic hibonite were interpreted in terms of the crystal structure. Such a study is enabled by the rigorous characterization of the synthetic hibonites by NPD (Doyle *et al*., 2014) and is particularly important for Ti-bearing hibonite as site geometry influences Ti K-edge XANES spectra (Waychunas, 1987) and the Ti-bearing sites in hibonite distort with increasing Ti content (Doyle *et al*., 2014).

Post-crest region – Ti K-edge XANES spectra of silicates and oxides characteristically have up to three peaks in the post-crest region (Waychunas, 1987). Similarly, three peaks are present in the post-crest region of the spectrum of the Ti^{3+} end-member hibonite sample (0.20,1). In contrast, spectra collected from Ti^{4+} end-member hibonites have four peaks (Fig. 4). Ti^{4+} occupies two site geometries in hibonite: the M2 trigonal bipyramidal site and the M4 octahedral site, which are connected by O3 (Doyle *et al*., 2014; Fig. 6). The combined effect of these substitutions, may account for the four peaks in the Ti^{4+}-bearing hibonite spectra.

Further evidence for the structural control of spectral features in the post-crest region of the spectra can be observed in the near-linear correlation of the d_2 peak intensity with Mg content (Fig. 7a), which is a proxy for Ti^{4+} pfu. In addition, the intensity of the m_2 minimum decreases as the proportion of Ti^{4+} on the M2 site increases (Fig. 7b).

Pre-edge region – The pre-edge peaks gain intensity by mixing of the Ti 3*d* and O 2*p* orbitals, which is enhanced at low symmetry (distorted) Ti sites (Brown *et al*., 1988), so changes in site geometry should be reflected in the shape of the pre-edge. For example, the pre-edge feature in spectra recorded from Ti in a symmetrical octahedral site is almost non-existent (Waychunas, 1987), and that of Ti^{4+} in tetrahedral coordination is comparable in intensity to the absorption edge (Farges *et al*., 1996).

Accordingly, with Ti^{4+} occupying the M2 trigonal bipyramidal site ($^{[5]}Ti^{4+}_{[M2]}$) as well as the M4 octahedral site ($^{[6]}Ti^{4+}_{[M4]}$), the pre-edge peaks of the Ti^{4+}-bearing hibonites should be more intense than those of the Ti^{3+} end-member samples ($^{[6]}Ti^{3+}_{[M4]}$). This is the case (Fig. 4), suggesting the a_2 peak height may be related to the $^{[5]}Ti^{4+}_{[M2]}/^{[6]}Ti^{tot}_{[M4]}$ ratio.

If the central pre-edge peak (a_2) intensity is dominated by site geometry, then as the $^{[5]}Ti^{4+}_{[M2]}/^{[6]}Ti^{tot}_{[M4]}$ ratio increases, so too should the a_2 pre-edge peak intensity. The a_2 intensities for the Ti^{4+} end-member hibonites in this study are within uncertainty, consistent

with the finding that Ti^{4+} partitions between the M2 and M4 sites with a constant ratio for these samples (Doyle *et al.*, 2014).

Ti^{4+} and Ti^{3+} in octahedral coordination also contribute to the pre-edge shape, and Ti in octahedral coordination is reported to have three peaks (Waychunas, 1987; Farges *et al.*, 1996). Three peaks are evident in the spectra of the Ti^{3+} end-member hibonite (Fig. 4), in which Ti^{3+} only occupies the M4 octahedral site (Doyle *et al.*, 2014). The a_1 and a_3 pre-edge peaks are more intense in the Ti^{4+} end-member hibonites than the Ti^{3+}-rich hibonites (Fig. 4). Furthermore, the a_3 peak intensity of (0.98,0) is 19% more intense than that of (0.44,0). These characteristics may be explained by distortion of the M4 site, which is coordinated by three O3 and three O5 (Fig. 6).

Bond-length ratios can be used as a measure of the distortion of a site, and an undistorted M4 site would have a M4-O3/M4-O5 ratio of 1. The M4-O3/M4-O5 ratios of the Ti^{3+} end-member hibonites (0.20,1) and (0.33,1) are 1.045 and 1.049, respectively (calculated from Doyle *et al.*, 2014). These values and the low pre-edge peak intensities are consistent with the Ti^{3+}-bearing M4 sites being relatively undistorted. The amount of distortion is roughly the same for these samples, and the spectra of (0.20,1) and (0.33,1) are similar (Supplementary Fig. 2).

In contrast, the Ti^{4+}-hibonites (0.44,0) and (0.98,0) have M4-O3/M4-O5 ratios of 1.058 and 1.103 respectively (calculated from Doyle *et al.*, 2014), such that the M4 site of (0.98,0) is almost twice as distorted as that of (0.44,0). As the distortions of the M2 and M4 sites vary as a function of Ti pfu (Doyle *et al.*, 2014), and the XANES spectra reflect Ti at both sites, it is useful to consider a ratio of the pre-edge peak intensities. For example, the a_2/a_3 intensity ratio is inversely correlated with M4-O3/M4-O5 (Fig. 8). This relationship, as well as the a_2 pre-edge peak intensity, indicates that the pre-edge peak intensities of hibonite are controlled by the coordination environment, site occupancy and distortion of the M2 and M4 Ti-bearing sites.

The pre-edge peaks for $^{[6]}Ti^{3+}$ are expected to occur at lower energy than those of $^{[6]}Ti^{4+}$ (Waychunas, 1987). The pre-edge peaks of $^{[5]}Ti^{4+}$ should also occur at lower energy than those of $^{[6]}Ti^{4+}$ (Farges *et al.*, 1996), yet across the series the a_2 peak shifts by <0.09 eV in a non-systematic manner (Table 2). The lack of pre-edge shift with changing $Ti^{3+}/\Sigma Ti$ within the energy resolution of this experiment may be due to the masking effect of Ti^{4+} substituting in both the five-fold coordinated M2 site and the six-fold coordinated M4 site.

This study therefore shows that the pre-edge parameters a_2 and a_3 of hibonite are controlled by both Ti coordination environment and distortion of the Ti-bearing sites. This is

consistent with the correlation between site distortion and the a_2 pre-edge peak intensity reported for silicate minerals (Waychunas, 1987).

Orientation study – Hibonite is an anisotropic mineral, so the absorption of a polarized X-ray beam may result in spectral variations due to the orientation of a crystal. Although orientation effects are observed in the post-crest region of spectra collected from Ti^{4+}-bearing hibonites, the pre-edge region does not seem to be affected by orientation. This may be due to the substitution of >80% of Ti on the M4 octahedral site. The face-sharing nature of the M4 site (Fig. 6) and the 180° rotation of the RS and R'S' blocks (Bermanec *et al.*, 1996; Doyle *et al.*, 2014) may also minimize orientation effects. Indeed, the deviation in pre-edge peak intensity observed for multiple spectra collected from a single Ti-bearing hibonite sample is less than the 10% that was reported for V K-edge XANES spectra collected from a single sample of the isotropic mineral spinel (Righter *et al.*, 2006).

In the post-crest region, orientation effects were observed in the spectra of the synthetic Ti^{4+}-bearing hibonites, but not in those of the Ti^{3+} end-member hibonites. Ti^{4+} occupies the M2 trigonal bipyramidal site, which has a long axis parallel to the c-axis (Fig. 6), irrespective of the stacking of the S and R blocks, and this may result in a greater orientation effect than for Ti^{3+} (or Ti^{4+}) on the M4 octahedral site. Alternatively, given that the structure of the post-crest region is influenced by next-nearest neighbor interactions (Brown *et al.*, 1988) and that orientation effects appear absent in the pre-edge region, substitution of Ti^{4+} on adjoining M2 and M4 sites may cause the orientation effects observed in the post-crest region.

If, as proposed above, Ti^{4+} on the M2 site is the cause of the orientation effects in the post-crest region, then one may expect orientation effects to be observed in the spectra collected from terrestrial hibonite BM 1966,28c. However, the spectra of BM 1966,28c show little variation in the post-crest region, and the characteristic d_2 peak of the Ti^{4+}-bearing hibonite spectra is weak (Supplementary Fig. 5). This may reflect increased complexity and site distortions associated with the incorporation of significant quantities of other substituting cations, such as Fe, Th and rare earth elements (REE) (Supplementary Table 2). For example, Fe preferentially occupies the M2 site in hibonite (Bermanec *et al.*, 1996; Holtstam, 1996; discussion in Doyle *et al.*, 2014), and both Th and the REE substitute onto the 12-fold coordinated Ca-bearing site (Bermanec *et al.*, 1996), which is located adjacent to M2 (Supplementary Fig. 1).

The absence of orientation effects in the pre-edge region of randomly orientated crystals of synthetic hibonite is encouraging. Future studies may wish to investigate orientation effects in Ti^{3+},Ti^{4+}-bearing hibonite using either large single crystals of synthetic hibonite or

meteoritic hibonite crystals having >2.5 wt% TiO_2, such as the biminerallic CAI fragment NWA 2446/5L (PL07041) that contains Ti-poor augite and hibonite (0.22 Ti pfu), as described by Rout and Bischoff (2008) and Doyle (2012).

4.3. Ti valence state calibration curve

The site occupancy of Ti in hibonite is different for Ti^{3+} and Ti^{4+} (Doyle *et al.*, 2014), and the geometries of the site(s) occupied by Ti determine the pre-edge peak shape (Waychunas, 1987; Farges *et al.*, 1996). The spectral lineshapes would therefore be expected to vary as a function of $Ti^{3+}/\Sigma Ti$. Indeed, as the value of $Ti^{3+}/\Sigma Ti$ in hibonite increases, the intensities of the pre-edge peaks decrease, and both the m_1 minimum and absorption edge shift to lower energy (Fig. 9).

Pre-edge peak intensities have previously been used to determine $Ti^{3+}/\Sigma Ti$ in meteoritic pyroxene (Simon *et al.*, 2007). The a_2 peak intensities of hibonite are, however, not suitable for developing a Ti valence calibration as Ti^{4+} in hibonite occupies two sites of different geometry and the pre-edge peak shape is influenced by site geometry, Ti-content and the resulting site distortion (Section 4.2). Secondly, as a maximum of 0.25 $Ti^{3+}/\Sigma Ti$ is reported for meteoritic hibonite (Simon *et al.*, 1997), a robust Ti^{4+} end-member parameter is required for any hibonite Ti valence state calibration curve, but the uncertainty of the a_2 peak intensity for $Ti^{3+}/\Sigma Ti = 0$ (Fig. 9a) would inhibit the accuracy of results obtained using this feature.

Spectral parameters that are related to $Ti^{3+}/\Sigma Ti$, irrespective of site occupancy, distortion and Ti content, would be ideal for a Ti valence calibration curve. The pre-edge feature and absorption edge occur at lower energies in Ti^{3+}- than Ti^{4+}-bearing materials (Waychunas, 1987), so greater consideration was given to the variation of these features as a function of $Ti^{3+}/\Sigma Ti$.

The energy of the absorption edge at an intensity of 0.8 ($E_{0.8}$) for Ti_2O_3 is ~5 eV lower than that of TiO_2 (Table 2) and, as expected, the $E_{0.8}$ energy for hibonite shifts to progressively lower energies with increasing $Ti^{3+}/\Sigma Ti$. The shift occurs in a non-linear manner (Fig. 9b).

The energy of the m_1 minimum (E_{m1}) also shifts to lower energy with increasing $Ti^{3+}/\Sigma Ti$ (Fig. 9c). A linear mixing model of the (0.20,1) Ti^{3+} and (0.44,0) Ti^{4+} end-member hibonite spectra reproduces the shift of the E_{m1} minimum to lower energy between these two end-members (Supplementary Fig. 6).

Peak fits of the pre-edge region (Supplementary Fig. 3) indicate that the m_1 minimum is an overlap point between the high energy tail of the pre-edge multiplet and the low energy tail of the main absorption edge. As the fraction of Ti^{3+} increases, the intensity of the a_3 pre-

edge component decreases, the b_1 component increases, and the main absorption edge shifts to lower energy, resulting in the m_1 minimum region narrowing (Fig. 4) and the m_1 minimum shifting to lower energy. The increase in the b_1 component with increasing $Ti^{3+}/\Sigma Ti$ (Supplementary Fig. 3b) suggests that E_{m1} may be more strongly influenced by b_1 than by the pre-edge peaks. As a result, E_{m1} should be controlled by the oxidation state of Ti, rather than the site geometry. This is supported by the E_{m1} of the two Ti^{4+} end-member hibonites being equal within uncertainty (Fig. 5b), despite having TiO_2 contents of 5.2 and 11.4 wt% TiO_2.

The correlation between $Ti^{3+}/\Sigma Ti$ and E_{m1} is shown in Figure 10 and the data is fit by a quadratic function. The curved form of the calibration may be due to the excitation of Ti^{4+} on both the M2 and M4 sites. Indeed, the contribution of $^{[5]}Ti^{4+}$ to the spectra will decrease as the $^{[5]}Ti^{4+}_{[M2]}/^{[6]}Ti^{tot}_{[M4]}$ ratio decreases with increasing substitution of Ti^{3+} on the M4 site in Ti^{3+}-bearing hibonites.

The correlation of the E_{m1} parameter with $Ti^{3+}/\Sigma Ti$ may be applicable to other mineral systems. For example, in Ti K-edge XANES spectra collected from synthetic clinopyroxenes grown at 1226-1234 ^{o}C and fO_2 ranging from IW to IW-5.7 (Paque *et al.*, 2013), the E_{m1} parameter appears to shift to lower energy for samples prepared under increasingly more reducing conditions. Ti^{3+} content is negatively correlated with fO_2 (Paque *et al.*, 2013: Table 1), so E_{m1} decreases with increasing Ti^{3+} content, as expected from the present study.

4.4. Application to meteoritic hibonites

The non-linear nature of the Ti valence calibration and the overlap in uncertainties for E_{m1} values with $Ti^{3+}/\Sigma Ti > 0.6$, indicate that the calibration curve for the oxidation state of Ti is most sensitive for hibonites with $Ti^{3+}/\Sigma Ti < 0.3$ (perhaps $Ti^{3+}/\Sigma Ti < 0.5$). This may be sufficient for the investigation of meteoritic hibonite as $Ti^{3+}/\Sigma Ti$ up to 0.25 has been reported for the CM2 Murchison carbonaceous chondrite (Simon *et al.*, 1997). The E_{m1} values for hibonite in CAI NWA 1476/124 from the R3 NWA 1476 chondrite predict $Ti^{3+}/\Sigma Ti$ up to 0.22 using this calibration (Doyle, 2012).

Crystal chemical controls may limit the Ti (and $Ti^{3+}/\Sigma Ti$) content of natural hibonite as, although up to 1.9 Ti^{3+} pfu was reported in synthetic single crystals of $Ca(Al,Ti)_{12}O_{19}$ grown as an impurity phase during an iron smelting process (Wittmann *et al.,* 1958), there has been no report of natural or synthetic hibonite with >1 Ti^{4+} pfu (Doyle, 2012). Indeed, the maximum reported Ti contents of meteoritic and terrestrial hibonite are similar, being 0.85 and 0.86 Ti pfu, respectively (Simon *et al.*, 1997; Rakotondrazafy *et al.*, 1996), while hibonites with up to ~1 Ti^{4+} pfu have been prepared (Doyle *et al.*, 2014; Giannini *et al.*, 2014). Synthesis of hibonite with more than 1 Ti^{4+} has been attempted: when the bulk

composition of the starting material was 1.25 Ti^{4+} pfu (Section 3.1), the proportion of Ti-bearing impurities in the product increased. Similarly, using a nominal composition of 2 Ti pfu prepared under oxidizing (IW+7.7) and reducing (IW-2.8) conditions, Giannini *et al.* (2014) reported single-crystal hibonite with 0.94 Ti^{4+} and 1.18 Ti^{tot} pfu, respectively. The latter sample is blue in color and, based on stoichiometry, contains 0.97 Ti^{4+} and 0.21 Ti^{3+} pfu.

If the Ti^{4+} content of hibonite is limited by crystal chemistry, then it may also restrict the upper $Ti^{3+}/\Sigma Ti$ ratio in natural hibonite, as suggested by Beckett *et al.* (1988). $Ti^{3+}/\Sigma Ti$ can be fixed by the stoichiometry of the starting mixture to give hibonite with $Ti^{3+}/\Sigma Ti$ ranging from 0 to 1 (Doyle *et al.*, 2014; Table 1), such that Ti^{4+} is stabilized under very reducing conditions (IW-6.5) due to the presence of Mg^{2+}. The role of Mg must therefore be considered, with the possibility that $Ti^{3+}/\Sigma Ti$ may be controlled by Mg due to the coupled substitution mechanism of Mg^{2+} and Ti^{4+}. Therefore, although a mechanism for quantifying $Ti^{3+}/\Sigma Ti$ in hibonite is proposed herein, correlating fO_2 with $Ti^{3+}/\Sigma Ti$ in hibonite is fraught with complexity. For example, in addition to Ti^{3+} being stable at different fO_2s for a suite of hibonite compositions (Ihinger and Stolper, 1986) and the complex crystal chemical control on Ti site occupancy, $Ti^{3+}/\Sigma Ti$ in hibonite may be influenced by the availability of Mg due to volatility; it may increase due to resorption and distillation processes; and/or be overprinted during thermal metamorphism, as discussed by Doyle (2012).

Therefore, of all the meteoritic hibonites, it is those from pristine condensates that are most likely to contain $Ti^{3+}/\Sigma Ti$ values that may be related to the fO_2 conditions of formation. The quantification of Ti^{3+} in hibonites from such samples, for which synthetic analogues have been prepared over a range of fO_2s, would provide the best indication of the redox conditions of CAI formation. A high energy resolution beamline, possibly with a Si(311) monochromator and/or analyzer crystal detector would be most ideal for obtaining accurate $Ti^{3+}/\Sigma Ti$ ratios of meteoritic hibonites using the E_{m1} parameter, for which the range in energy is ~1 eV for $Ti^{3+}/\Sigma Ti$ from 0 to 1. Moreover, as minor differences in the reference energies would significantly alter the results, Ti K-edge XANES spectra of hibonite standards and the "unknowns" should be collected during the same experimental session.

5. Conclusion

Synthetic hibonites with 2.4-11.4 wt% TiO_2 were prepared as standards for meteoritic hibonite. The largest yield of both Ti-free and Ti-bearing hibonite at ~1300 and/or ~1400 ^oC was obtained by a single sinter under reducing conditions.

Ti K-edge XANES spectra were collected from synthetic hibonites with $Ti^{3+}/\Sigma Ti$ ranging from 0 to 1. The intensities of the spectral peaks and minima are controlled by the Ti and Mg contents, the Ti coordination environment, site distortions and/or Ti oxidation state, whereas the energies of spectral parameters such as $E_{0.8}$ and E_{m1} appear to be controlled by the oxidation state of Ti.

Pre-edge peak intensities have previously been used to determine $Ti^{3+}/\Sigma Ti$ in meteoritic minerals. However, the pre-edge peak intensity for hibonite is affected by Ti occupying two different coordination environments and variable distortions of those Ti-bearing site(s). Parameters such as the pre-edge peak intensity of Ti K-edge XANES spectra should therefore be used with caution when constructing $Ti^{3+}/\Sigma Ti$ valence state calibration curves.

The energy of the minimum between the pre-edge and absorption edge (E_{m1}) in Ti K-edge XANES spectra may be used to quantify $Ti^{3+}/\Sigma Ti$ in meteoritic hibonite where ΣTi is sufficient to enable spectra with suitable signal-to-noise statistics to be recorded (e.g. >1 wt% TiO_2). The E_{m1} parameter may be determined from the first derivative of a spectrum, and the relationship between $Ti^{3+}/\Sigma Ti$ and E_{m1} can be modelled by a quadratic function. The Ti valence calibration is most reliable for hibonites with $Ti^{3+}/\Sigma Ti$ <0.3, and beamlines with sufficient energy resolution and reproducibility are needed. Furthermore, for accurate results, Ti K-edge XANES spectra must be collected from the synthetic hibonite standards and the meteoritic hibonites of interest during the same analytical session.

Acknowledgments

PMD gratefully acknowledges funding for a PhD studentship from the Natural History Museum (PI: PFS) and the Engineering and Physical Sciences Research Council (CASE/CNA/07/35, PI: AJB). The XANES experiments were facilitated by beamtime awards from the Diamond Light Source (NT490 and NT1175, PI: JFWM; and SP4516, PI: PFS), and the South African National Research Foundation is acknowledged for Postdoctoral Funding facilitating further work (grant #88191; PI: PMD). For technical support we thank Jack Nolan, Graham Nash, Tony Wighton, John Spratt and Anton Kearsley. We thank Associate Editor A.N. Krot and two anonymous reviewers for comments and suggestions that have helped improve this manuscript.

References

Allen, J.M., Grossman, L., Davis, A.M., Hutcheon, I.D., 1978. Mineralogy, textures and mode of formation of a hibonite-bearing Allende inclusion. *Proc. 9th Lunar Planet. Sci. Conf.*, 1209-1233.

Armstrong, J.T., Meeker, G.P., Huneke, J.C., Wasserburg, G.J., 1982. The Blue Angel: I. The mineralogy and petrogenesis of a hibonite inclusion from the Murchison meteorite. *Geochim. Cosmochim. Acta* **46**, 575-595.

Bearden, J.A. and Burr, A.F., 1967. Re-evaluation of X-ray atomic energy levels. *Rev. Mod. Phys.* **39**, 125-142.

Beckett, J.R., Live, D., Tsay, F.-D., Grossman, L., Stolper, E., 1988. Ti^{3+} in meteoritic and synthetic hibonite. *Geochim. Cosmochim. Acta* **52**, 1479-1495.

Bermanec, V.V., Holtstam, D., Sturman, D., Criddle, A.J., Back, M.E., Scavnicar, S., 1996. Nezilovite, a new member of the magnetoplumbite group, and the crystal chemistry of magnetoplumbite and hibonite. *Can. Mineral.* **34**, 1287-1297.

Berry, A.J., Danyushevsky, L.V., O'Neill, H.S.C., Newville, M., Sutton, S.R., 2008. Oxidation state of iron in komatiitic melt inclusions indicates hot Archaean mantle. *Nature* **455**, 960-963.

Berry, A.J. and O'Neill, H.S.C., 2004. A XANES determination of the oxidation state of chromium in silicate glasses. *Am. Min.* **89**, 790-798.

Berry, A.J., O'Neill, H.S.C., Jayasuriya, K.D., Campbell, S.J., Foran, G.J., 2003. XANES calibrations for the oxygen state of iron in a silicate glass. *Am. Min.* **88**, 967-977.

Berry, A.J., Walker, A.M., Hermann, J., O'Neill, H.S.C., Foran, G.J., Gale, J.D., 2007. Titanium substitution mechanisms in forsterite. *Chem. Geol.* **242**, 176-186.

Bischoff, A. and Srinivasan, G., 2003. ^{26}Mg excess in hibonites of the Rumuruti chondrite Hughes 030. *Meteorit. Planet. Sci.* **38**, 5-12.

Brown, G.E., Calas, G.J., Waychunas, G.A., Petiau, J., 1988. X-ray absorption spectroscopy and its applications in mineralogy and geochemistry. *Min. Soc. Am. Rev. Miner. Geochem.* **18**, 431-512.

Burns, R.G. and Burns, V.M. (1984) Crystal chemistry of meteoritic hibonites. *J. Geophys. Res.* **89**, 313-321.

Burnham, A.D., Berry, A.J., Halse, H.R., Schofield, P.F., Cibin, G., and Mosselmans, J.F.W. 2015 The oxidation state of europium in silicate melts as a function of oxygen fugacity, composition and temperature. *Chem Geol*, **411**, 248-259.

Callender, R.l., Barron, A.R., 2000. Facile synthesis of aluminum-containing mixed-metal oxides using doped carboxylate alumoxane nanoparticles. *J. Am. Ceram. Soc.* **83**, 1777-1789.

Connelly, J.N., Bizzarro, M., Krot, A.N., Nordlund, Å., Wielandt, D., Ivanova, M.A., 2012. The absolute chronology and thermal processing of solids in the Solar protoplanetary disk. *Science* **338**, 651-655

Davis, A.M., Tanaka, T., Grossman, L., Lee, T., Wasserburg, G.J., 1982. Chemical composition of HAL, an isotopically-unusual Allende inclusion. *Geochim. Cosmochim. Acta* **46**, 1627-1651.

De Aza, A.H., Iglesias, J.E., Pena, P., De Aza, S., 2000. Ternary System Al_2O_3-MgO-CaO: Part II, Phase relationships in the subsystem Al_2O_3-MgO-CaO. *J. Am. Ceram. Soc.* **83**, 919-927.

Domínguez, C., Chevalier, J., Torrecillas, R., Fantozzi, G., 2001. Microstructure development in calcium hexaluminate. *J. Eur. Ceram. Soc.* **21**, 381-387.

Doyle (2012) Ti substitution mechanisms in hibonite and the determination of Ti^{3+}/Ti^{4+} by X-ray absorption spectroscopy for use as an oxybarometer with application to early Solar System processes. *PhD thesis.* Imperial College London.

Doyle, P.M., Schofield, P.F., Berry, A.J., Walker, A.M., Knight, K.S., 2014. Substitution of Ti^{3+} and Ti^{4+} in hibonite ($CaAl_{12}O_{19}$). *Am. Min.* **99**, 1369-1382.

Dyl, K.A., Simon, J.I., Young, E.D., 2011. Valence state of titanium in the Wark-Lovering rim of a Leoville CAI as a record of progressive oxidation in the early Solar Nebula. *Geochim. Cosmochim. Acta* **75**, 937-949.

Farges, F. and Brown, G.E., 1997. Coordination chemistry of titanium (IV) in silicate glasses and melts: IV. XANES studies of synthetic and natural volcanic glasses and tektites at ambient temperature and pressure. *Geochim. Cosmochim. Acta* **61**, 1863-1870.

Farges, F., Brown, G.E., Rehr, J.J., 1996. Coordination chemistry of Ti(IV) in silicate glasses and melts .1. XAFS study of titanium coordination in oxide model compounds. *Geochim. Cosmochim. Acta* **60**, 3023-3038.

Fuchs, L.H., Olsen, E., Jensen, K.J., 1973. Mineralogy, mineral-chemistry, and composition of the Murchison (C2) Meteorite. *SM Con. Earth Sci.* **10**, 1-39.

Geiger, C.A., Kleppa, O.J., Mysen, B.O., Lattimer, J.M., Grossman, L., 1988. Enthalpies of formation of $CaAl_4O_7$ and $CaAl_{12}O_{19}$ (hibonite) by high temperature, alkali borate solution calorimetry. *Geochim. Cosmochim. Acta* **52**, 1729-1736.

Giannini, M., Ballaran Tiziana, B., Langenhorst, F., 2014. Crystal chemistry of synthetic Ti-Mg-bearing hibonites: A single-crystal X-ray study, *Am. Min.* **99**, 2060-2067.

Grossman, L., Beckett, J.R., Fedkin, A.V., Simon, S.B., Ciesla, F.J., 2008. Redox conditions in the solar nebula: observational, experimental, and theoretical constraints. *Min. Soc. Am. Rev. Miner. Geochem.* **68**, 93-140.

Haggerty, S.E., 1978. The Allende meteorite: evidence for a new cosmothermometer based on Ti^{3+}/Ti^{4+}. *Nature* **276**, 221-225.

Henke, B.L., Gullikson, E.M., Davis, J.C., 1993. X-ray interactions: photoabsorption, scattering, transmission, and reflection at E=50-30000 eV, Z=1-92. *Atom. Data Nucl. Data* **54** 181-342. (http://henke.lbl.gov/optical_constants/atten182.html; 2011).

Hofmeister, A.M., Wopenka, B., Locock, A.J., 2004. Spectroscopy and structure of hibonite, grossite, and $CaAl_2O_4$: Implications for astronomical environments. *Geochim. Cosmochim. Acta* **68**, 4485-4503.

Holtstam, D., 1996. Iron in hibonite: a spectroscopic study. Phys. *Chem. Miner.* **23**, 452-460

Ihinger, P.D. and Stolper, E., 1986. The color of meteoritic hibonite: an indicator of oxygen fugacity. *Earth Planet. Sci. Lett.* **78**, 67-79.

Ireland, T.R., 1988. Correlated morphological, chemical, and isotopic characteristics of hibonites from the Murchison carbonaceous chondrite. *Geochim. Cosmochim. Acta* **52**, 2827-2839.

Ireland, T.R., 1990. Presolar isotopic and chemical signatures in hibonite-bearing refractory inclusions from the Murchison carbonaceous chondrite. *Geochim. Cosmochim. Acta* **54**, 3219-3237.

Kita, N.T., Yin, Q.-Z., MacPherson, G.J., Ushikubo, T., Jacobsen, B., Nagashima, K., Kurahashi, E., Krot, A.N., Jacobsen, S.B., 2013. ^{26}Al-^{26}Mg isotope systematics of the first solids in the early solar system. *Meteorit. Planet. Sci.* **48**, 1383-1400.

Krause, M. and Oliver, J.H., 1979. Natural widths of atomic K and L levels, Kα X-ray lines and several KLL Auger lines. *J. Phys. Chem. Ref. Data* **8**, 329-338.

Krawczynski, M.J., Sutton, S.R., Grove, T.L., Newville, M., 2009. Titanium oxidation state and coordination in the lunar high-titanium glass source mantle, *40th Lunar Planet. Sci.* Lunar Planet. Inst., Houston. #2164 (Abstract).

Krot, A., McKeegan, K., Huss, G., Liffman, K., Sahijpal, S., Hutcheon, I., 2006. Aluminium-magnesium and oxygen isotope study of relict Ca-Al-rich inclusions in chondrules. *Astrophys. J.* **639**, 1227-1237.

Krot, A.N., Fagan, T.J., Keil, K., Mckeegan, K.D., Sahijpal, S., Hutcheon, I.D., Petaev, M.I., Yurimoto, H., 2004. Ca,Al-rich inclusions, amoeboid olivine aggregates, and Al-rich chondrules from the unique carbonaceous chondrite Acfer 094: I. mineralogy and petrology. *Geochim. Cosmochim. Acta* **68**, 2167-2184.

Lodders, K., 2003. Solar System abundances and condensation temperatures of the elements. *Astrophys. J.* **591**, 1220-1247.

Mosselmans J.F.W., Quinn P.D., Roque Rosell J., Atkinson K.D., Dent A.J., Cavill S.I., Hodson M.E., Kirk C.A., Schofield P.F., 2008. The first environmental science experiments on the new microfocus spectroscopy beamline at Diamond. *Min. Mag.* **72**, 197-200.

Mosselmans, J.F.W., Quinn, P.D., Dent, A.J., Cavill, S.A., Moreno, S.D., Peach, A., Leicester, P.J., Keylock, S.J., Gregory, S.R., Atkinson, K.D., Rosell, J.R., 2009. i18 – the microfocus spectroscopy beamline at the Diamond Light Source. *J. Synchrotron Radiat.* **16**, 818-824.

MSDS (2016) e.g. LTS Research Laboratories material safety data sheets (MSDS): TiO_2, Ti_2O_3, TiO at http://www.ltschem.com/msds/

Paque, J.M., Sutton, S.R., Simon, S.B., Beckett, J.R., Burnett, D.S., Grossman, L., Yurimoto, H., Itoh, S., Connolly, H.C., 2013. XANES and Mg isotopic analyses of spinels in Ca-Al-rich inclusions: Evidence for formation under oxidizing conditions. *Meteorit. Planet. Sci.* **48**, 2015-2043.

Rakotondrazafy, M.A.F., Moine, B., Cuney, M., 1996. Mode of formation of hibonite ($CaAl_{12}O_{19}$) within the U-Th skarns from the granulites of S-E Madagascar. *Contrib. Min. Pet.* **123**, 190-201.

Righter, K., Sutton, S.R., Newville, M., Le, L., Schwandt, C.S., Uchida, H., Lavina, B., Downs, R.T., 2006. An experimental study of the oxidation state of vanadium in spinel and basaltic melt with implications for the origin of planetary basalt. *Am. Min.* **91**, 1643-1656.

Rout, S.S., Bischoff, A., Nagashima, K., Krot, A.N., Huss, G.R., Keil, K. (2009) Oxygen- and magnesium-isotope compositions of calcium-aluminum-rich inclusions from Rumuruti (R) chondrites. *Geochim. Cosmochim. Acta* **73**, 4264-4287.

Schofield, P.F., Knight, K.S., Covey-Crump, S.J., Cressey, G., Stretton, I.C., 2002. Accurate quantification of the modal mineralogy of rocks when image analysis is difficult. *Min. Mag.* **66**, 189–200.

Schofield, P.F., Smith, A.D., Mosselmans, J.F.W., Ohldag, H., Scholl, A., Raoux, S., Cressey, G., Cressey, B.A., Quinn, P.D., Kirk, C.A., Hogg, S.C., 2010. X-ray spectromicroscopy of mineral intergrowths in the Santa Catharina meteorite. *Geostand. Geoanal. Res.* **34**, 145-159.

Schofield, P.F., Smith, A.D., Scholl, A., Doran, A., Covey-Crump, S.J., Young, A.T., Ohldag, H., 2014. Chemical and oxidation-state imaging of mineralogical intergrowths: The application of X-ray photo-emission electron microscopy (XPEEM). *Coordin Chem Rev* 277–278, 31-43.

Schreiber, H.D., Thanyasiri, T., Lach, J.J., Legere, R.A., 1978. Redox equilibria of Ti, Cr, and Eu in silicate melts: reduction potentials and mutual interactions. *Phys. Chem. Glasses* **19**, 126-139.

Simon, J.I., Young, E.D., Russell, S.S., Tonui, E.K., Dyl, K.A., Manning, C.E., 2005. A short timescale for changing oxygen fugacity in the solar nebula revealed by high-resolution ^{26}Al-^{26}Mg dating of CAI rims. *Earth Planet. Sci. Lett.* **238**, 272-283.

Simon, S.B., Grossman, L., Davis, A.M., 1991. Fassaite composition trends during crystallization of Allende Type B refractory inclusion melts. *Geochim. Cosmochim. Acta* **55**, 2635-2655.

Simon, S.B., Grossman, L., Davis, A.M., 1997. Multiple generations of hibonite in spinel-hibonite inclusions from Murchison. *Meteorit. Planet. Sci.* **32**, 259-269.

Simon, S.B., Sutton, S.R., Grossman, L., 2007a. Valence of titanium and vanadium in pyroxene in refractory inclusion interiors and rims. *Geochim. Cosmochim. Acta* **71**, 3098-3118.

Simon, S.B., Sutton, S.R., Grossman, L., 2007b. The valence of titanium in refractory forsterite, *38th Lunar Planet. Sci.* Lunar Planet. Inst., Houston. #1892 (Abstract).

Simon, S.B., Sutton, S.R., Grossman, L., 2009. First Ti-XANES analyses of refractory inclusions from Murchison, *40th Lunar Planet. Sci.* Lunar Planet. Inst., Houston. #1626 (Abstract).

Smith, A.D., Schofield, P.F., Cressey, G., Cressey, B.A., Read, P.D., 2004. The development of X-ray photo-emission electron microscopy (XPEEM) for valence-state imaging of mineral intergrowths. *Min. Mag.* **68**, 859–869.

Stoyanov, E., Langenhorst, F., Steinle-Neumann, G., 2007. The effect of valence state and site geometry on Ti $L_{3,2}$ and O K electron energy-loss spectra of Ti_xO_y phases. *Am. Min.* **92**, 577-586.

Sutton, S.R., Karner, J., Papike, J., Delaney, J.S., Shearer, C., Newville, M., Eng, P., Rivers, M., Dyar, M.D., 2005. Vanadium K edge XANES of synthetic and natural basaltic glasses and application to microscale oxygen barometry. *Geochim. Cosmochim. Acta* **69**, 2333-2348.

Tranell, G., Ostrovski, O., Jahanshahi, S., 2002. The equilibrium partitioning of titanium between Ti^{3+} and Ti^{4+} valency states in CaO-SiO_2-TiO_x slags. *Metall. Mater. Trans. B* **33**, 61-67.

Ushikubo, T., Hiyagon, H., Sugiura, N., 2007. A FUN-like hibonite inclusion with a large ^{26}Mg-excess. *Earth Planet. Sci. Lett.* **254**, 115-126.

van Aken, P.A. and Liebscher, B., 2002. Quantification of ferrous/ferric ratios in minerals: new evaluation schemes of Fe L_{23} electron energy-loss near-edge spectra. *Phys. Chem. Miner.* **29**, 188-200.

Vázquez, B.A., Caballero, A., Pena, P., 2003. Quaternary System Al_2O_3-CaO-MgO-SiO_2: I, Study of the Crystallization Volume of Al_2O_3. *J. Am. Cer. Soc.* 86, 2195-2199.

Waychunas, G.A., 1987. Synchrotron radiation XANES spectroscopy of Ti in minerals: effects of Ti bonding distances, Ti valence, and site geometry on absorption edge structure. *Am. Min.* **72**, 89-101.

Weber, D. and Bischoff, A., 1994. The occurrence of grossite ($CaAl_4O_7$) in chondrites. *Geochim. Cosmochim. Acta* **58**, 3855-3877.

Whipple, E.R., 1979. Errors in chemical analysis of two titanian micas. *Am. Min.* **64**, 1311.

Wittmann, A., Seifert, K. and Nowotny, H. (1958) Ein Beitrag zum Aufbau des Kalzium-Titan(III)-Aluminats. *Monatshefte für Chemie* **89**, 225-228. (Translated by Rudolf Umlat while based at Imperial College London).

Yang, X.C., Dubiel, M., Ehrt, D., Schütz, A.U.C., 2008. X-ray absorption near edge structure analysis of valence state and coordination geometry of Ti ions in borosilicate glasses. *J. Non-Cryst. Solids* **354**, 1172–1174.

Yoneda, S. and Grossman, L., 1995. Condensation of CaO-MgO-Al_2O_3-SiO_2 liquids from cosmic gases. *Geochim. Cosmochim. Acta* **59**, 3413-3444.

Doyle *et al.* GCA Submission – Figure captions

Fig. 1 Cations per formula unit (pfu) in synthetic and meteoritic hibonite: (A) Ti as a function of Mg; (B) Ti and Mg as a function of Al; and (C) Ti, Si, Mg and Fe as a function of Al, Cr and V. The dashed lines indicate the expected stoichiometric relationship between the cations ($y = 12 - x$). The meteoritic data are from Fuchs *et al*. (1973), Allen *et al*. (1978), Armstrong *et al*. (1982), Davis *et al*. (1982), Burns and Burns (1984), Ireland (1988), Weber and Bischoff (1994), Simon *et al*. (1997), Bischoff and Srinivasan (2003), Krot *et al*. (2004), Krot *et al*. (2006), Ushikubo *et al*. (2007), Rout *et al*. (2009) and Doyle (2012).

Fig. 2 Backscatter electron images of (A, B) the Ti-poor and (C,D) the Ti-rich, Ti^{4+} and Ti^{3+} end-member hibonites.

Fig. 3 Ti K-edge XANES spectra for reference materials: Ti-olivine ($^{[4]}$Ti-ol), Ti-spinel ($^{[4]}$Ti-sp), $^{[6]}TiO_2$ and $^{[6]}Ti_2O_3$. (A) The main peaks are marked for the pre-edge region (a, or a_1, a_2, a_3), the absorption edge (b_1, b_2, b_3), crest (c) and post-crest region (d_1, d_2, d_3); (B) the pre-edge region with the main peaks marked (a, or a_1, a_2, a_3). Spectra are offset for clarity.

Fig. 4 (A) Ti K-edge XANES spectra and (B) pre-edge region for the synthetic hibonite suite: the Ti^{4+} end-member hibonites (0.98,0) and (0.44,0), the mixed-valent hibonites (0.62,0.60) and (0.73,0.33), and the Ti^{3+} end-member hibonite (0.20,1). The main peaks (a-d) and minima (m) are marked and the spectra are offset for clarity.

Fig. 5 (A) a_2 pre-edge peak intensity and (B) energy of the m_1 minimum as a function of Ti per formula unit (pfu). Uncertainties (1 standard deviation) based on 6-10 spectra and 26-42 EDS SEM analyses.

Fig. 6 A portion of the hibonite structure showing the M2 trigonal bipyramidal site and two adjacent M4 octahedral sites. The M2 cation is axially displaced from the equatorial plane and connected to two M4 cations by O3. The hibonite structure is shown in more detail in Supplementary Fig. 1.

Fig. 7 Spectral parameters from the post-crest region: (A) intensity of the d_2 peak as a function of Mg pfu (a proxy for Ti^{4+} pfu); and (B) intensity of the post-crest m_2 minimum as

a function of the proportion of Ti on the M2 trigonal bipyramidal site. Structural data from Doyle *et al*. (2014). The d_2 intensity for (0.20,1) is the intensity at the d_2 energy of the other samples. Uncertainties in spectral parameters are the standard deviation of 6-10 spectra.

Fig. 8 The a_2/a_3 intensity ratio as a function of the bond-length ratio M4-O3/M4-O5, which is a measure of the distortion of the M4 octahedral site.

Fig. 9 (A) Intensity of the a_2 peak, (B) energy of the absorption edge at intensity 0.8 ($E_{0.8}$) and (C) energy of the m_1 minimum (E_{m1}) as a function of $Ti^{3+}/\sum Ti$ in synthetic hibonite, Ti_2O_3 and TiO_2. The arrows point to off-scale positions of spectral values.

Fig. 10 $Ti^{3+}/\Sigma Ti$ of synthetic hibonite as a function of E_{m1} (Table 2) fitted with a quadratic function.

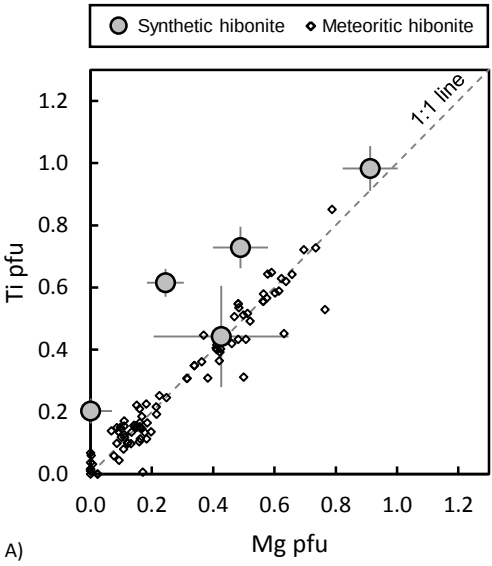
Synthetic hibonite
Meteoritic hibonite
1:1 line
Ti pfu
Mg pfu
0.0
0.2
0.4
0.6
0.8
1.0
1.2

A)

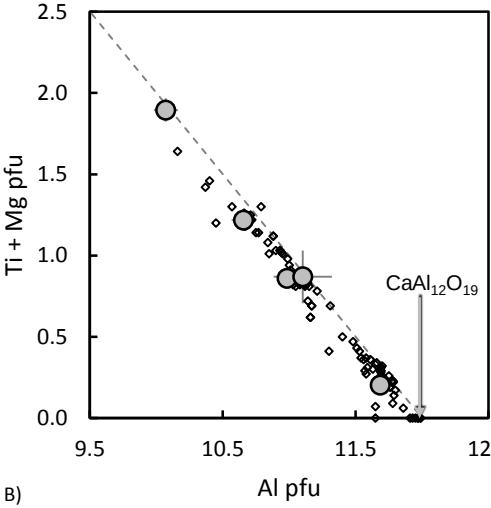
Ti + Mg pfu
Al pfu
CaAl12O19
0.0
0.5
1.0
1.5
2.0
2.5
9.5
10.5
11.5
12.5

B)

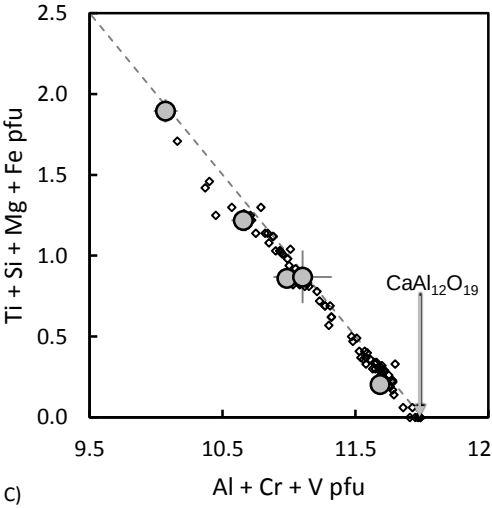
Ti + Si + Mg + Fe pfu
Al + Cr + V pfu
CaAl12O19
0.0
0.5
1.0
1.5
2.0
2.5
9.5
10.5
11.5
12.5

C)

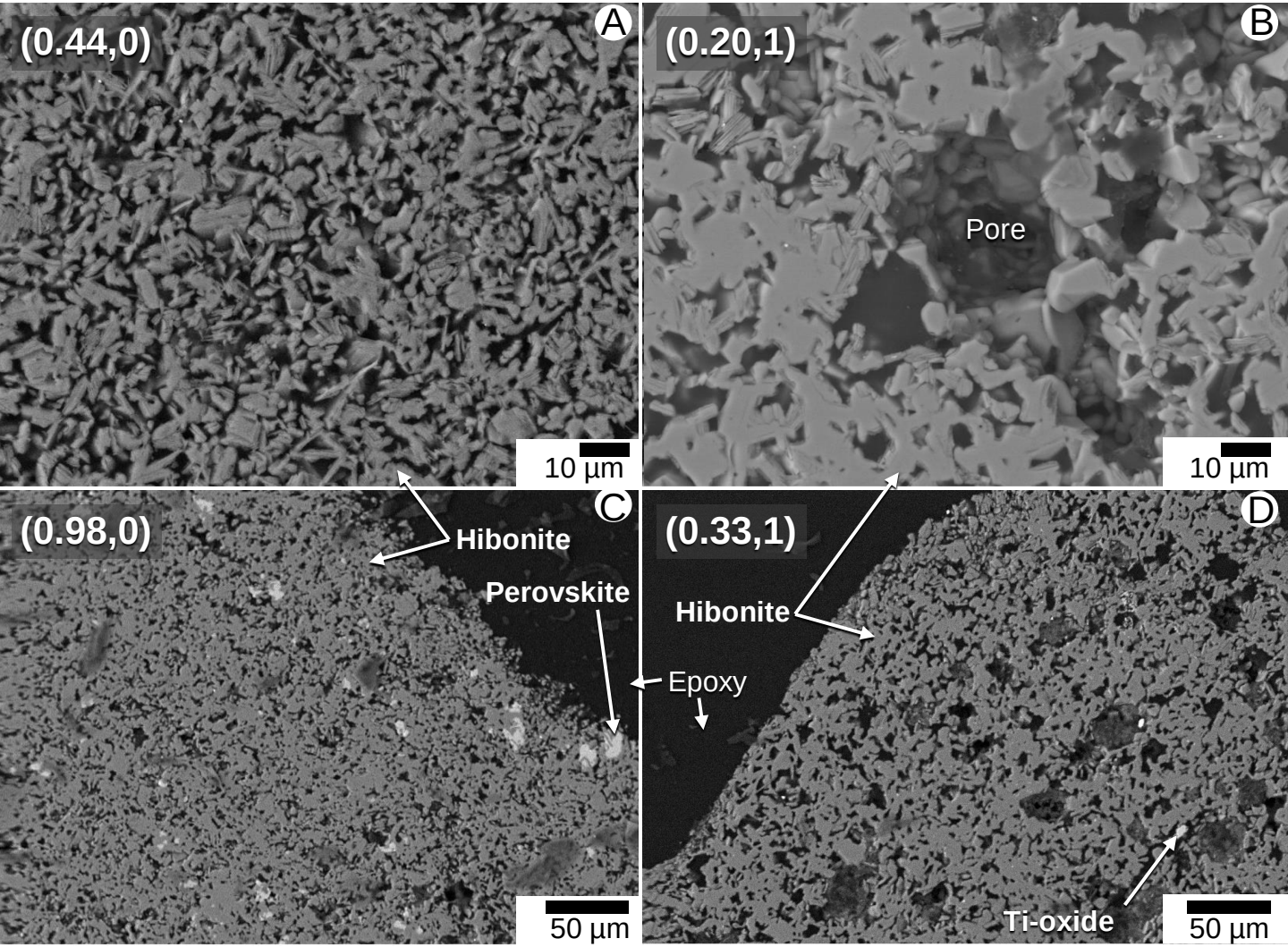
(0.44,0)
A
10 µm
(0.20,1)
B
Pore
10 µm
(0.98,0)
C
Hibonite
Perovskite
50 µm
(0.33,1)
D
Hibonite
Epoxy
Ti-oxide
50 µm

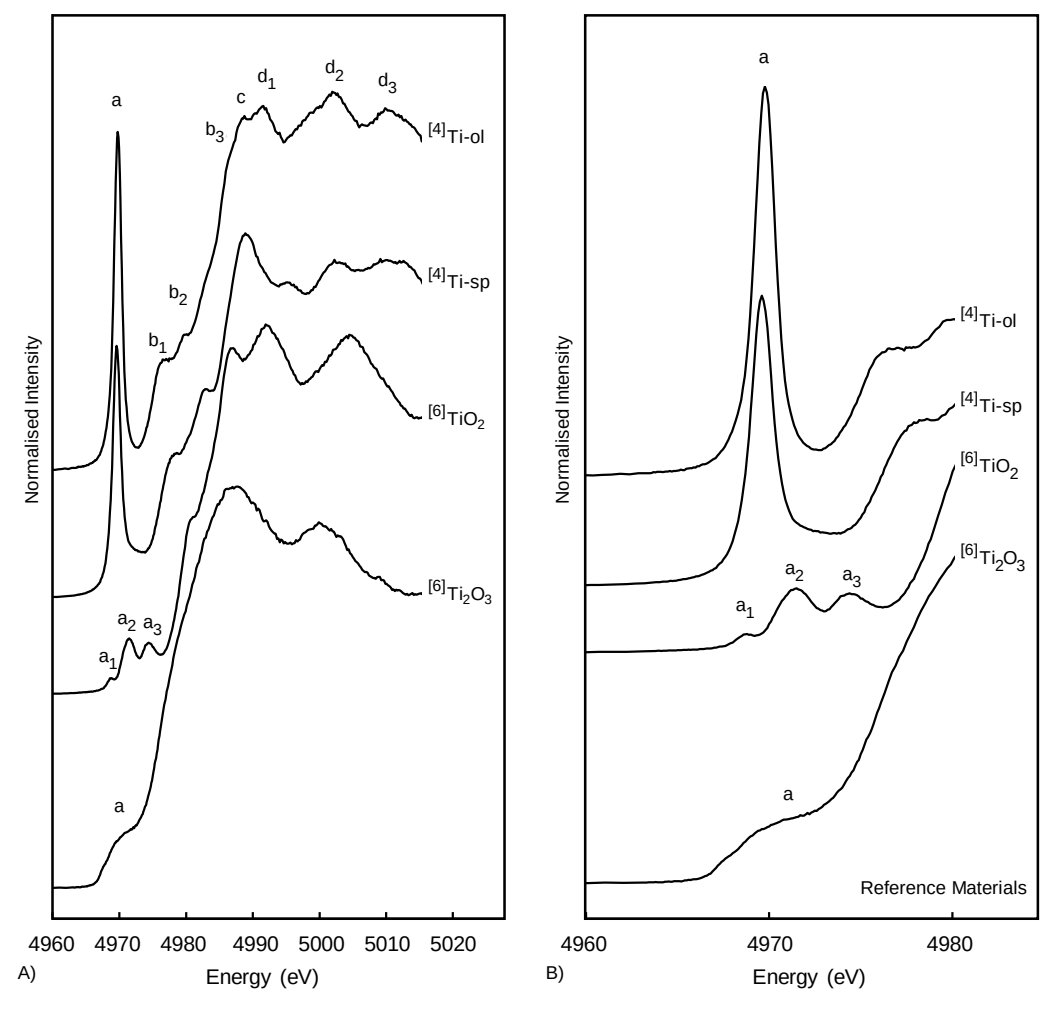
a
b3
c
d1
d2
d3
[4]Ti-ol
b2
[4]Ti-sp
b1
[6]TiO2
[6]Ti2O3
a1
a2
a3
a
Normalised Intensity
4960
4970
4980
4990
5000
5010
5020
Energy (eV)
A)
a
[4]Ti-ol
[4]Ti-sp
[6]TiO2
[6]Ti2O3
a2
a3
a1
a
Reference Materials
Normalised Intensity
4960
4970
4980
Energy (eV)
B)

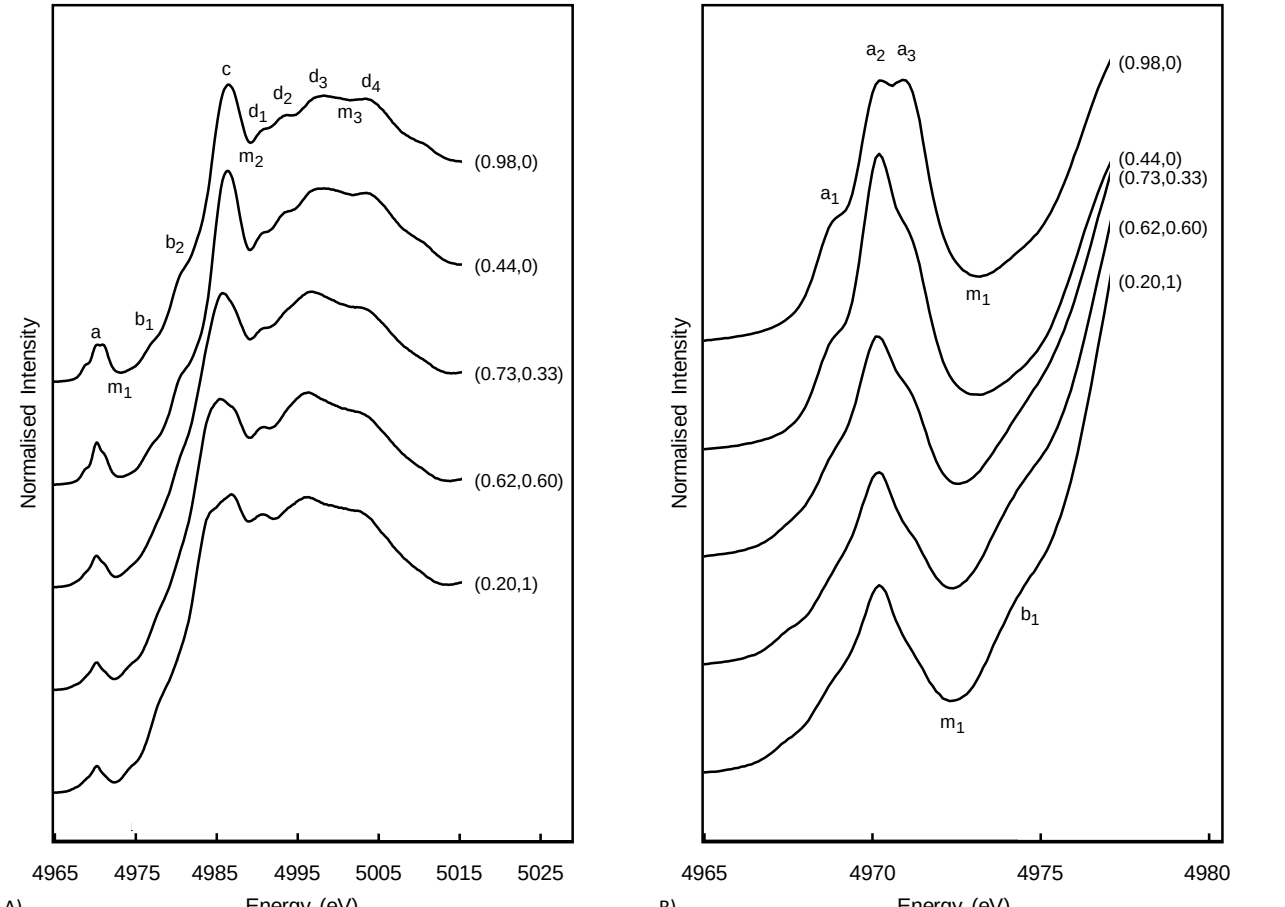
Normalised Intensity
a
m1
b1
b2
c
m2
d1
d2
d3
m3
d4
(0.98,0)
(0.44,0)
(0.73,0.33)
(0.62,0.60)
(0.20,1)
4965
4975
4985
4995
5005
5015
5025
Energy (eV)
A)
Normalised Intensity
a1
a2
a3
m1
b1
m1
(0.98,0)
(0.44,0)
(0.73,0.33)
(0.62,0.60)
(0.20,1)
4965
4970
4975
4980
Energy (eV)
B)

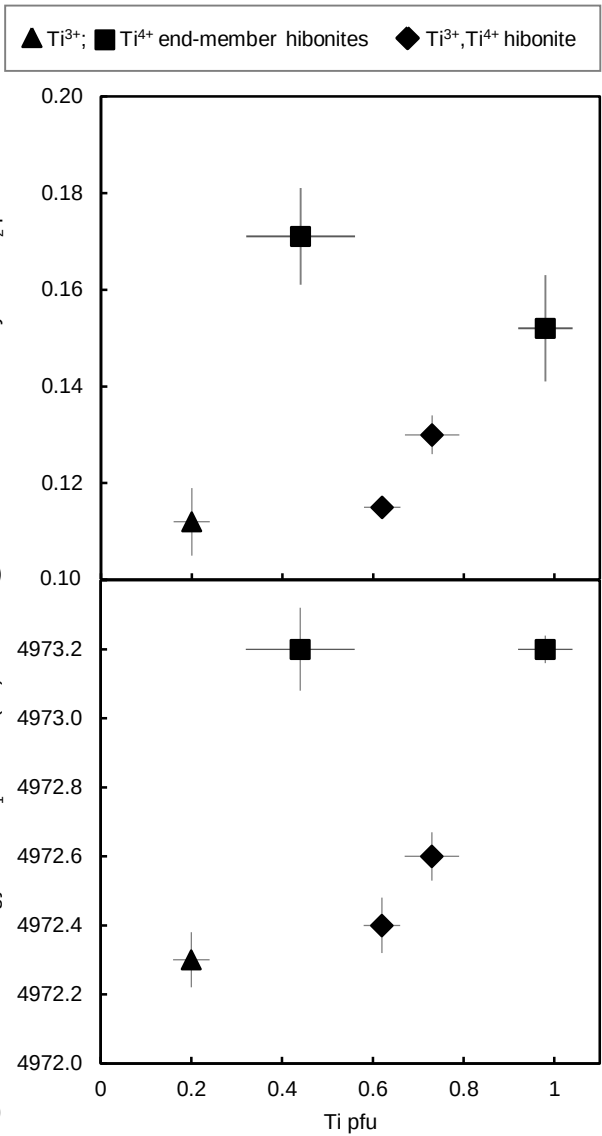
Ti3+; Ti4+ end-member hibonites
Ti3+,Ti4+ hibonite
Intensity of the a2 peak
0.20
0.18
0.16
0.14
0.12
0.10
A)
Energy of the m1 feature (eV)
4973.2
4973.0
4972.8
4972.6
4972.4
4972.2
4972.0
0
0.2
0.4
0.6
0.8
1
B)
Ti pfu

c

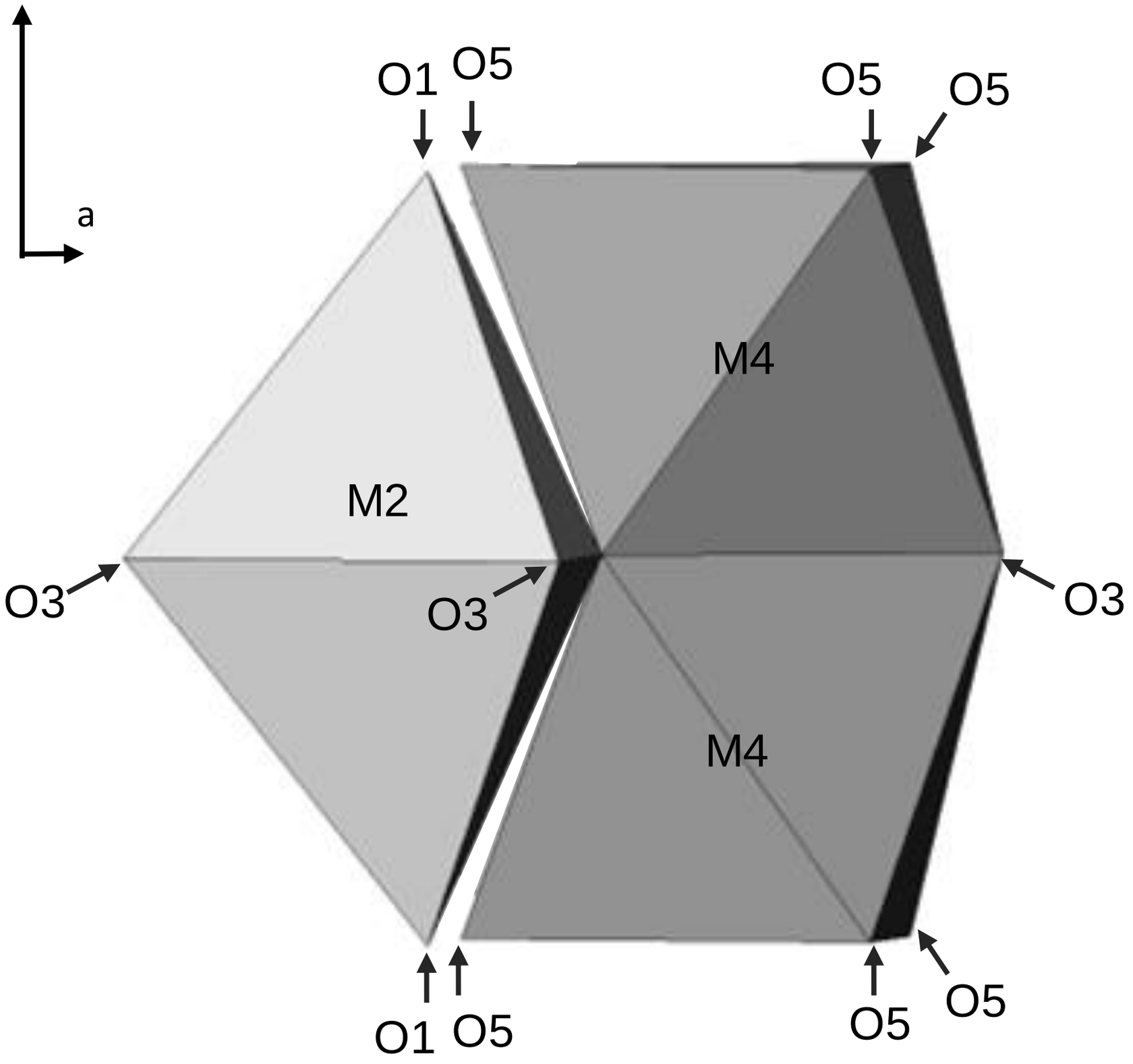

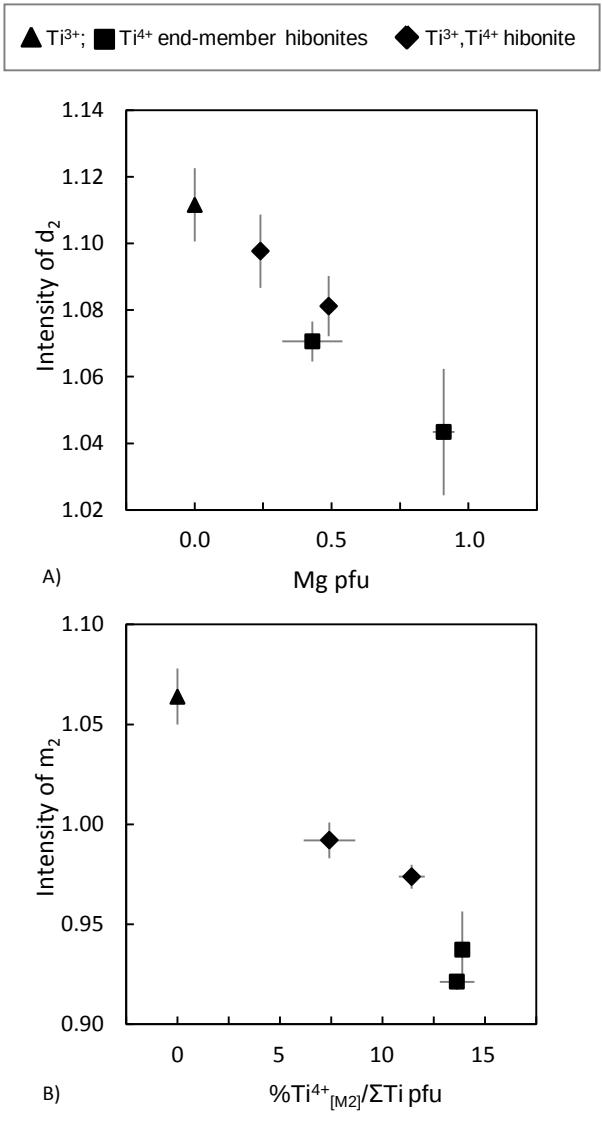
Ti3+; Ti4+ end-member hibonites
Ti3+,Ti4+ hibonite
1.14
1.12
1.10
1.08
1.06
1.04
1.02
Intensity of d2
0.0
0.5
1.0
Mg pfu
A)
1.10
1.05
1.00
0.95
0.90
Intensity of m2
0
5
10
15
%Ti4+[M2]/ΣTi pfu
B)

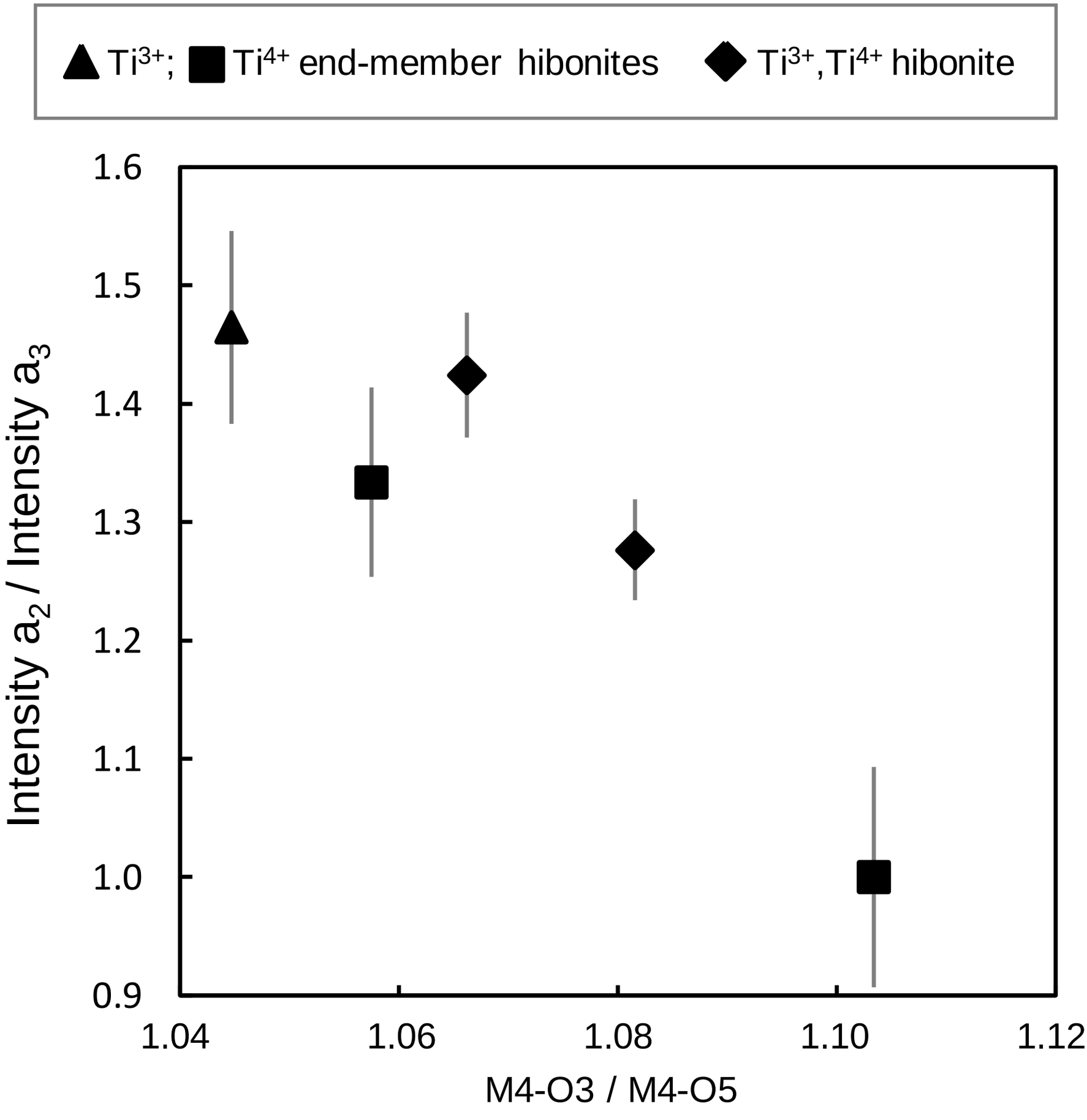
Ti3+; Ti4+ end-member hibonites
Ti3+,Ti4+ hibonite
1.6
1.5
1.4
1.3
1.2
1.1
1.0
0.9
Intensity a2 / Intensity a3
1.04
1.06
1.08
1.10
1.12
M4-O3 / M4-O5

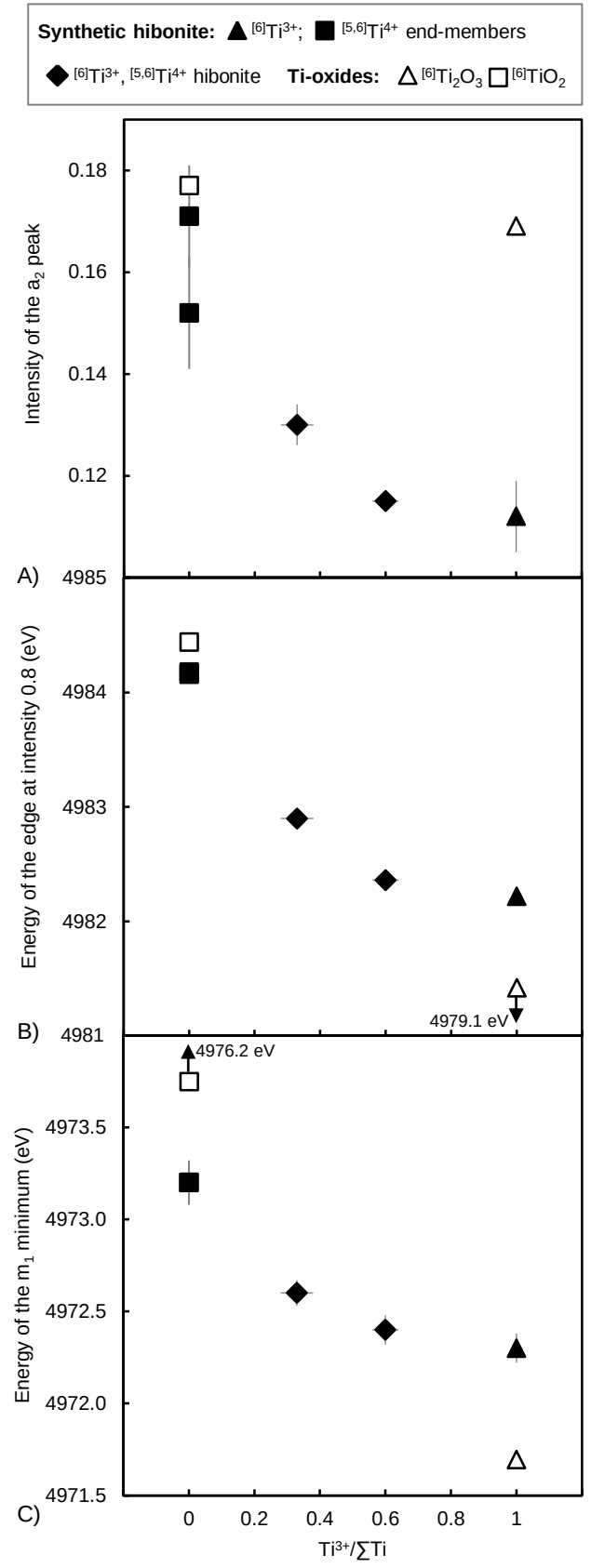
Synthetic hibonite: [6]Ti3+; [5,6]Ti4+ end-members
[6]Ti3+, [5,6]Ti4+ hibonite
Ti-oxides: [6]Ti2O3 [6]TiO2
Intensity of the a2 peak
0.18
0.16
0.14
0.12
A)
4985
Energy of the edge at intensity 0.8 (eV)
4984
4983
4982
4981
B)
4979.1 eV
4976.2 eV
Energy of the m1 minimum (eV)
4973.5
4973.0
4972.5
4972.0
4971.5
C)
0
0.2
0.4
0.6
0.8
1
Ti3+/∑Ti

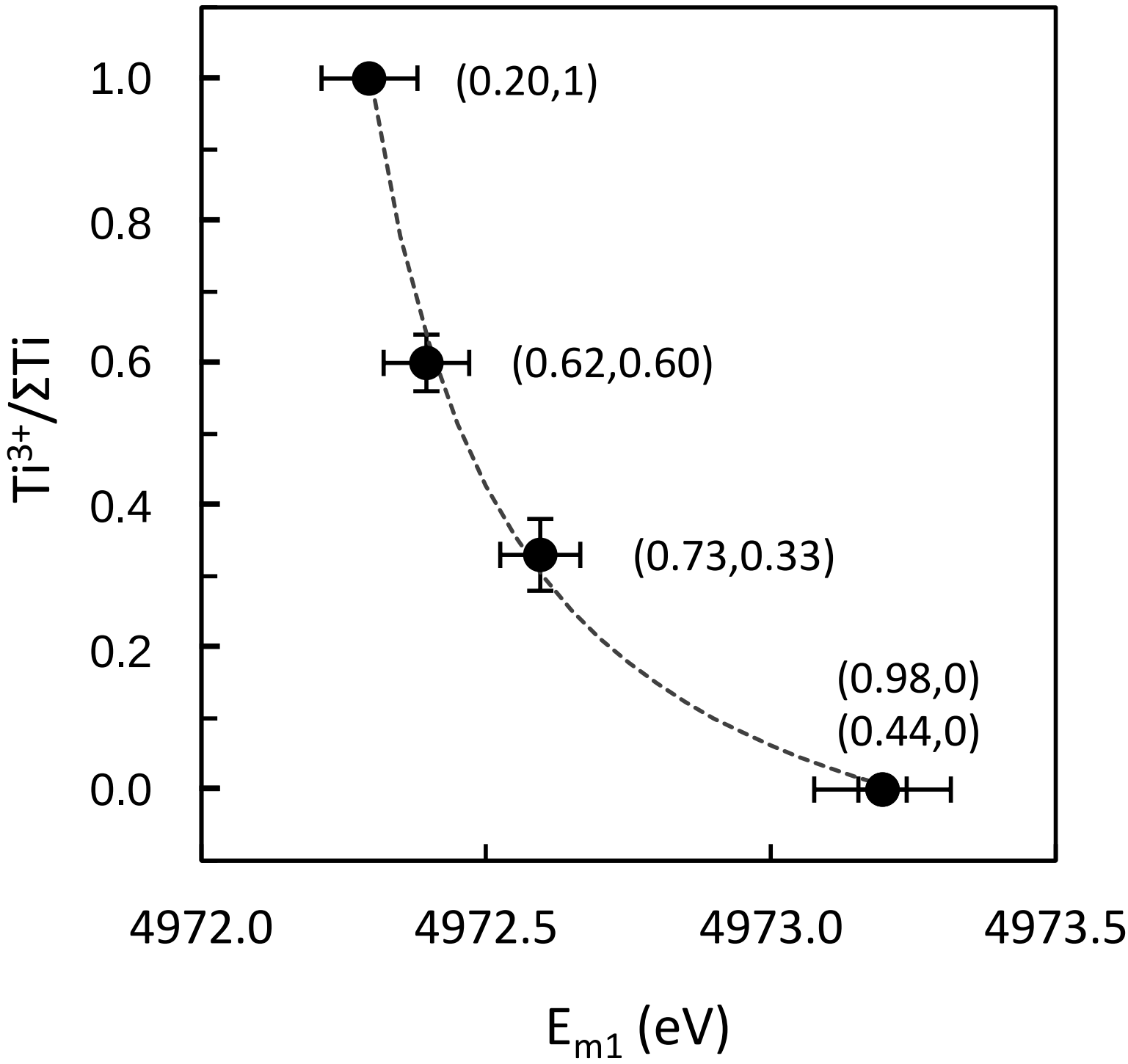
1.0
0.8
0.6
0.4
0.2
0.0
$Ti^{3+}/\Sigma Ti$
(0.20,1)
(0.62,0.60)
(0.73,0.33)
(0.98,0)
(0.44,0)
4972.0
4972.5
4973.0
4973.5
E_{m1} (eV)

Doyle *et al.* Table 1

Table 1 Synthetic hibonite compositions: oxide weight%, cation proportions and $Ti^{3+}/\Sigma Ti$

Sample	wt% oxide					Number of cations normalized to 19 O					$Ti^{3+}/\Sigma Ti$	#
	CaO	Al_2O_3	TiO_2^{tot}	MgO	Total	Ca	Al	Ti	Mg	Total Cations	Calculated	
(0.20,1)	8.8 ±0.4	88.2 ±0.6	2.4 ±0.5	<lld	**99.4** ±0.7	1.07 ±0.04	11.69 ±0.07	0.20 ±0.04	<lld	**12.95** ±0.02	1	37
(0.62,0.60)	8.7 ±0.3	82.8 ±0.5	7.3 ±0.5	1.5 ±0.1	**100.2** ±0.7	1.05 ±0.04	10.99 ±0.06	0.62 ±0.04	0.24 ±0.02	**12.89** ±0.02	0.60 ±0.04	27
(0.73,0.33)	8.8 ±0.3	79.9 ±1.0	8.6 ±0.7	2.9 ±0.2	**100.2** ±0.9	1.07 ±0.03	10.66 ±0.09	0.73 ±0.06	0.49 ±0.03	**12.94** ±0.02	0.33 ±0.05	42
(0.98,0)	8.3 ±0.4	74.8 ±0.7	11.4 ±0.7	5.4 ±0.2	**100.0** ±0.9	1.01 ±0.04	10.07 ±0.09	0.98 ±0.06	0.91 ±0.04	**12.98** ±0.03	0	28
(0.44,0)	8.5 ±0.3	83.0 ±1.9	5.2 ±1.4	2.5 ±0.6	**99.2** ±0.6	1.04 ±0.03	11.10 ±0.22	0.44 ±0.12	0.43 ±0.11	**13.01** ±0.02	0	26
(0.33,1)	8.8 ±0.3	86.7 ±0.6	4.0 ±0.4	<lld	**99.5** ±0.8	1.07 ±0.04	11.51 ±0.05	0.33 ±0.04	<lld	**12.91** ±0.02	1	30
(0.46,0.10)	8.6 ±0.3	82.8 ±1.9	5.4 ±0.6	2.4 ±0.5	**99.2** ±0.7	1.05 ±0.03	11.08 ±0.23	0.46 ±0.13	0.40 ±0.09	**13.00** ±0.02	0.10 ±0.12	31

Notes: The sample nomenclature is in the form (Ti pfu, $Ti^{3+}/\Sigma Ti$). One standard deviation. # = Number of EDS SEM analyses. "lld" = lower limit of detection.

Doyle *et al.* Table 2

Table 2 Ti K-edge XANES spectral parameters for synthetic hibonite and Ti-oxides

Sample	a_2 (I)		a_2 (E, eV)		E_{m1} (E, eV)		$E_{0.8}$ (E, eV)		#
(0.20,1)	0.112	±0.007	4970.20	±0.05	4972.30	±0.08	4982.22	±0.04	10
(0.62,0.60)	0.115	±0.002	4970.21	±0.08	4972.40	±0.08	4982.36	±0.03	6
(0.73,0.33)	0.130	±0.004	4970.16	±0.05	4972.60	±0.07	4982.90	±0.06	10
(0.44,0)	0.171	±0.010	4970.20	±0.00	4973.20	±0.12	4984.18	±0.03	10
(0.98,0)	0.152	±0.010	4970.24	±0.05	4973.20	±0.04	4984.16	±0.07	10
Ti_2O_3	0.169		4970.90		4971.70		4979.11		1
TiO_2	0.177		4971.49		4976.20		4984.44		1

965 Note: Parameter values from an average of # spectra. One standard deviation.